Modeling the Influence of Intrinsic Dipole Field Strength and Interplanetary Magnetic Field Orientation on Ion Escape from Weakly Magnetized Planets

by

Julianna Cessna

Bachelor of Arts – Department of Astrophysical & Planetary Sciences

Undergraduate Honors Thesis

Final Copy

Thesis Defense Committee:

Prof. David Brain	Thesis Advisor	Department of APS
Prof. David Malaspina	Honors Council Representative	Department of APS
Prof. Michael Litos	Outside Reader	Department of Physics

Defended on:

April 10, 2023

This thesis entitled:
Modeling the Influence of Intrinsic Dipole Field Strength and Interplanetary Magnetic Field Orientation on Ion Escape from Weakly Magnetized Planets
written by Julianna Cessna
has been approved for the Department of Astrophysical & Planetary Sciences

Prof. David Brain

Prof. David Malaspina

Prof. Michael Litos

Date

The final copy of this thesis has been examined by the signatories, and we find that both the content and the form meet acceptable presentation standards of scholarly work in the above mentioned discipline.

Cessna, Julianna (Astronomy)

Modeling the Influence of Intrinsic Dipole Field Strength and Interplanetary Magnetic Field Orientation on Ion Escape from Weakly Magnetized Planets

Thesis directed by Prof. David Brain

For a planet to be deemed habitable, it must have a substantial atmosphere. Planetary and stellar properties are common drivers for atmospheric loss in planets. A planetary property whose role in atmospheric loss has been called into question is the presence and strength of a planet's dipole magnetic field. A stellar property that interacts directly with this planetary property is the magnetic field that is embedded in the solar wind, called the interplanetary magnetic field (IMF). The orientation of the IMF (clock angle and cone angle) relative to the dipole field influences magnetospheric configuration and the importance of kinetic effects within the plasma. The interaction between the two fields determine the trajectories of atmospheric particles near the planet, thereby affecting atmospheric loss.

In this project, we use a global hybrid plasma model to simulate atmospheric ion loss from a Mars-like planet while changing the surrounding magnetic environment. We begin with a 'base case' of a magnetized planet with an IMF orientation that is perpendicular to the dipole field axis. The clock angle and cone angle of the base case are varied independently to determine the IMF orientation influence on ion escape. Then, the intrinsic dipole field strength of the planet is varied from nonmagnetized to magnetized to determine its dependence on ion loss through all explored IMF orientations. We find that the weakly magnetized planet is most influenced by IMF clock angle and the nonmagnetized and magnetized planets are most influenced by IMF cone angle.

Dedication

To Ben and Andy. Thank you for giving me a reason to stay. Love you.

Acknowledgements

There are certain people I must thank for their help over the course of this project. First, I must thank my advisor, Dave, for being an understanding mentor and pushing me to grow as a confident scientist through my employment at LASP. I must also thank Yaxue for her help and encouragement through this project, as well as Neesha for their support and advice. And of course, I also thank my parents, my sister Natalie, and my partner Dan for lifting me up through this whole process. I couldn't have done it with out you all and I am so thankful for you.

This work utilized the Alpine high performance computing resource at the University of Colorado Boulder. Alpine is jointly funded by the University of Colorado Boulder, the University of Colorado Anschutz, Colorado State University, and the National Science Foundation (award 2201538).

Contents

Chapter

Tables

Table

Figures

Figure

Chapter 1

Introduction

Out of all the worlds that populate the universe, which ones can potentially sustain a life form like ours? Since human civilization began, we have been searching for an answer to the question “are we alone?”. The search for extraterrestrial life has the goal of finding a planet that has hospitable conditions for life. Such conditions include a substantial atmosphere that can maintain liquid water on its surface, since liquid water is the foundation of all life on Earth. For liquid water to remain stable on the surface, the atmosphere has to maintain enough pressure so the water does not immediately evaporate. Collisions of atmospheric particles generate atmospheric pressure. To maintain a substantial atmosphere to support liquid water, there must be enough atmospheric particles and subsequent collisions. Therefore, atmospheric retention and evolution play a critical role in a planet’s ability to support life.

Atmospheric retention for habitable planets is a delicate balancing act. Adding too much or too little atmosphere can be detrimental. When there is too much atmosphere added, the high atmospheric pressure leads to a hostile environment where liquid water and life cannot exist, as seen at Venus with its incredibly high surface temperature. On the other hand, too little pressure due to atmospheric loss produces an environment that is vulnerable to solar radiation, as seen at Mars. Of the many atmospheric loss processes, I have chosen to focus on the process of charged particles in the planetary upper atmosphere escaping to space. In this project, we focus on the atmospheric loss processes that produce atmospheric conditions that are in the ‘Goldilocks’ zone, just like on Earth.

Planetary properties as well as stellar properties dictate atmospheric conditions. Planetary properties include characteristics such as size, rotation rate, orbital distance, and atmospheric composition. A property whose role has been recently questioned is the presence and strength of an intrinsic magnetic field. The fact that Earth has retained an atmosphere that keeps liquid water in a stable phase on the surface is sometimes attributed to its strong global magnetic field [18]. Based on atmospheric observations of unmagnetized and weakly magnetized planets, this role of a planet’s magnetic field is less certain [14]. This calls for further investigation as to whether intrinsic magnetic fields play a role in atmospheric retention for non-magnetized and weakly magnetized planets.

Stellar properties that control atmospheric conditions include the Extreme Ultraviolet (EUV) flux, the solar wind, and the interplanetary magnetic field (IMF) embedded in the solar wind. High EUV fluxes can increase atmospheric loss by heating and energizing planetary atmospheres, leading to atmospheric ion escape [8]. The IMF carried by the solar wind interacts with the planet’s magnetic environment and controls the trajectories of charged particles near the planet. Specifically, the orientation of the IMF relative to the planetary magnetic field may influence atmospheric escape [8, 16, 17].

1.1 Magnetospheres

Before we can analyze ion escape from planetary atmospheres, we must first define the magnetic environment that controls the process of ion loss.

Every planetary body, whether magnetized or unmagnetized, interacts with the incoming solar wind. All planets in our solar system have a disturbed region of space around them called a magnetosphere. A magnetosphere is a magnetic structure around a conducting planet that forms a protective cavity that results from planetary and stellar properties, such as an intrinsic dipole magnetic field and the solar wind [5]. There are two types of magnetospheres that form when considering conducting planetary bodies with atmospheres:

intrinsic and induced.

Intrinsic magnetospheres are formed from global magnetic fields intrinsic to the planet. A planet's global magnetic field is generated by a planet's convecting molten core and can be approximated as a dipole field. The magnetic field lines from the dipole field generate a magnetospheric structure that is shaped by the solar wind. When the solar wind interacts with a planetary magnetic field, the incoming solar wind slows down at a region called the bow shock, which is where the planetary charged particles interact with the solar wind charged particles [5]. The solar wind plasma is diverted around the planet at a boundary called the magnetopause, which is a boundary that separates the planetary plasma from the solar wind. As the solar wind flows around the planet, it stretches out the planetary magnetic field on the night side of the planet, forming the magnetotail. The magnetospheric structure is shown in Figure 1.1.

Conducting unmagnetized bodies do not have a convecting molten core to produce intrinsic magnetic fields, resulting in the atmosphere interacting with the solar wind instead of a global magnetic field. When solar radiation particles bombard the upper atmosphere, neutral atoms are photoionized, creating an ionosphere which interacts with the incoming solar wind. The ions accelerated by the electric field in the solar wind generate currents that prevent the IMF from diffusing through the unmagnetized body [5]. This interaction generates an induced magnetosphere, which is observed at Mars through MAVEN observations [7]. Induced magnetospheres have the same boundaries that intrinsically generated magnetospheres have.

The orientation of the IMF can change the structure of the planetary magnetosphere. When the IMF is parallel to the direction of the planetary dipole field lines, the magnetosphere remains relatively undisturbed. This results in a closed magnetospheric configuration where planetary dipole field lines start and stop at the surface of the planet, protecting the planetary plasma from the incoming solar wind plasma (see left panel of Figure 1.2).

When the IMF is oriented antiparallel to the planetary dipole field, the opposing topolo-

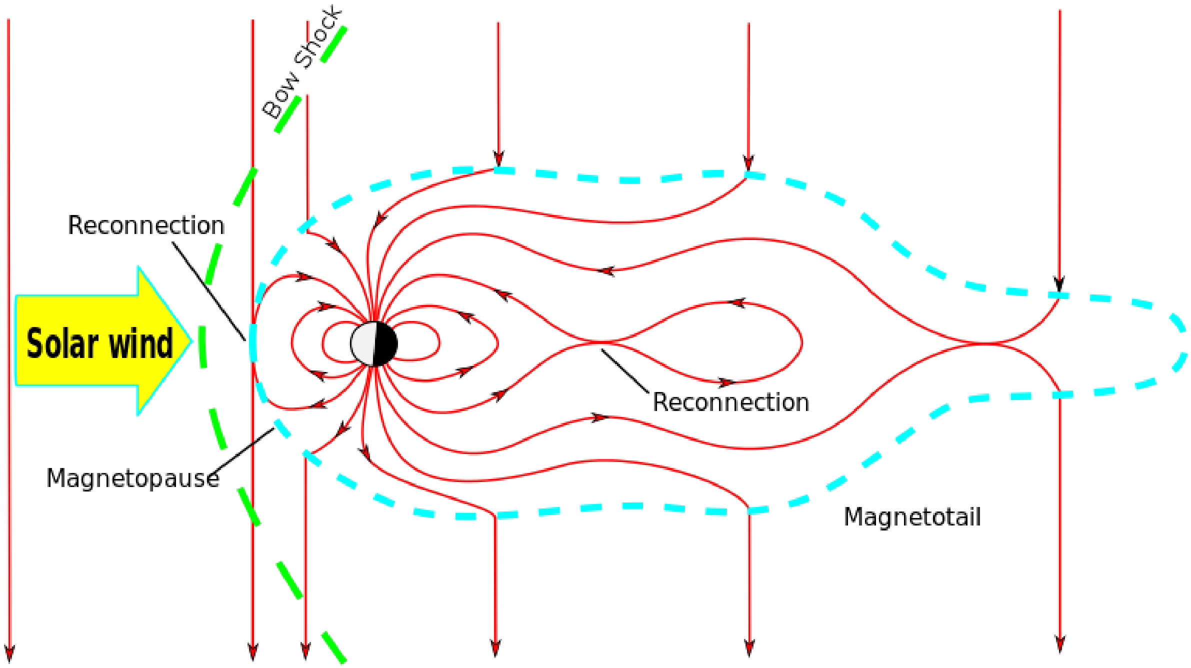

Figure 1.1: Courtesy of Wikimedia Commons. Schematic diagram of a planetary magnetosphere with the bow shock (where the solar wind slows down), magnetoause (boundary between planetary and solar wind plasma), and magnetotail (region of stretched out dipole field lines on the nightside). Probable areas of magnetic reconnection are also annotated on the dayside and within the magnetotail. Link: https://commons.wikimedia.org/wiki/File:Magnetopause.svg

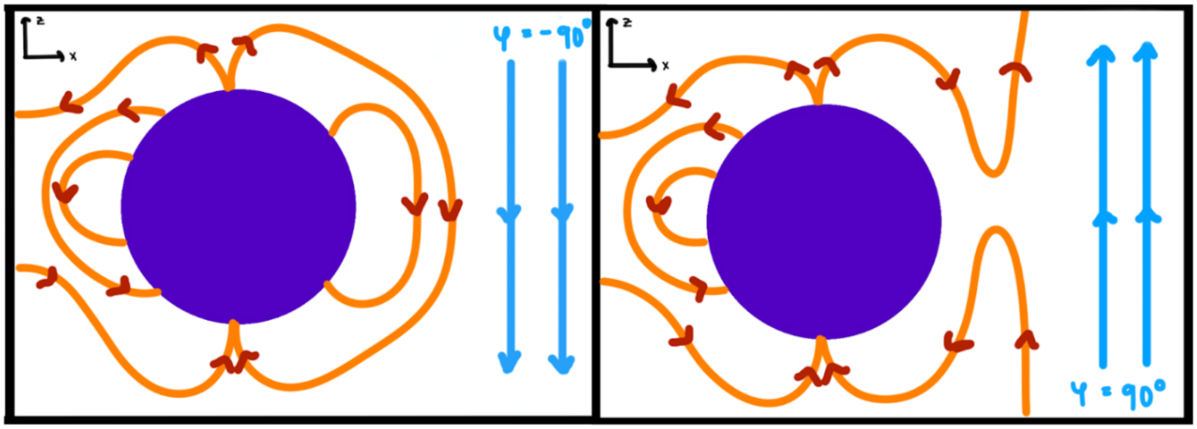

Figure 1.2: Schematic illustration of closed (left) and open (right) magnetospheric configurations, dependent on the relative orientation of the IMF (blue) with the planetary dipole field (orange).

gies of the fields have a high chance of magnetic reconnection on the dayside of the planet. Magnetic reconnection occurs when antiparallel magnetic field lines 'break and join together,' accelerating plasma away from the reconnection point (see Figure 1.3).

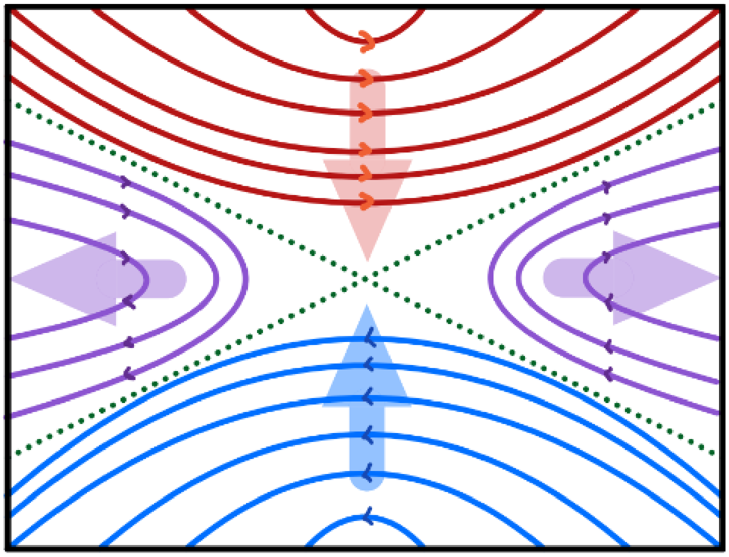

Figure 1.3: Schematic illustration showing process of magnetic reconnection of antiparallel magnetic field lines (red and blue lines) around a reconnection point (green dotted lines) and accelerated away from the reconnection point as conjoined field lines (purple).

This results in an open magnetospheric configuration, connecting the planetary dipole field lines to the IMF (right panel of Figure 1.2). Open magnetospheric configurations provide a pathway for planetary ions that connects to interplanetary space, thereby increasing the chance of atmospheric ion loss.

When the IMF cone angle is oriented parallel to the magnetospheric field lines, the chance of magnetic reconnection is very low due to compatible field topologies, leaving its configuration closed as the IMF drapes around the magnetosphere (see left panel of Figure 1.4). When the IMF is radial (parallel or antiparallel with incoming solar wind), as in the right panel of Figure 1.4, the magnetic structure of the planet disintegrates, resulting in the importance of kinetic effects.

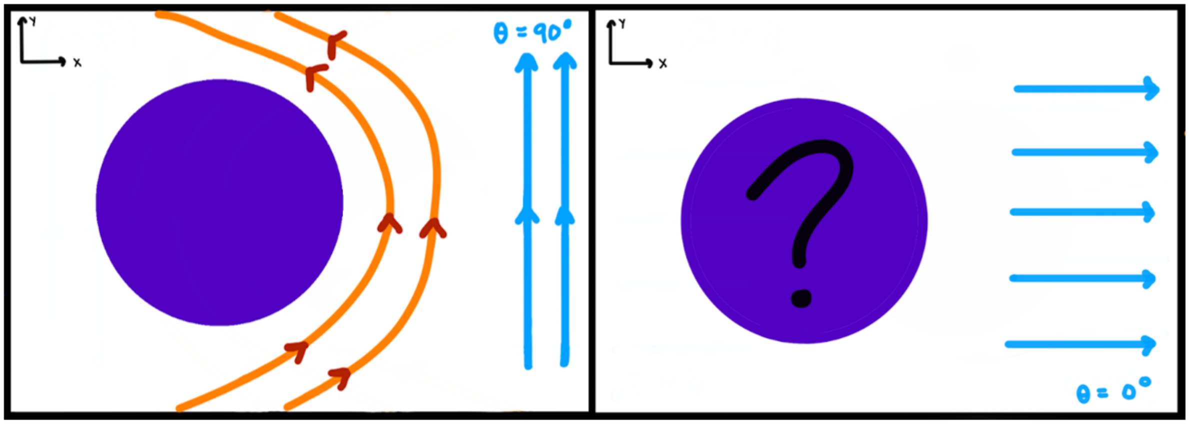

Figure 1.4: Schematic illustration of closed (left) magnetospheric configuration and when the IMF (blue) is parallel to the lanetary dipole field (orange). Radial IMF dependence on magnetospheric configuration (right) is unknown.

1.2 Ion Loss

The IMF orientation and resulting magnetospheric configuration can influence the ion loss processes from a planetary atmosphere. The process of planetary ion escape involves three separate stages, which are ion production, ion energization, and then ion escape.

Ion production begins in a neutral atmosphere that undergoes photoionization when Extreme Ultraviolet (EUV) photons from the star strip electrons from the atoms, creating an ionosphere. Ion energization entails the atmospheric ions being accelerated past the planet's escape velocity. Electric fields provide charged particles within the magnetosphere with enough energy to accelerate them out of the atmosphere. Three electric fields are the main drivers of ion energization: the convection electric field, the Hall field, and the electron pressure gradient. The convection electric field is the main driver for pickup ion escape and is present when the incoming solar wind plasma is not aligned with the IMF in the upstream region. The Hall field is prominent in induced magnetospheres with draped IMF [3]. In this case, the magnetic field lines 'want' to straighten out, accelerating the plasma away from the planet. The electron pressure gradient is only important close to the planet in the ionosphere. The electrons move quickly upwards through the ionosphere, driven by a pressure gradient. The plasma wants to stay quasineutral, so the ions are also accelerated upwards. An in-depth review of ion energization mechanism is available in Brain et al. (2016) [3]. Regardless of the energization mechanism, for an ion to escape from the planetary atmosphere, it must have enough energy to surpass the escape velocity of the planet. If it has enough energy, the ion will travel along open magnetic field lines that connect to interplanetary space and escape.

1.3 Observational and Modeling Results

It is often assumed that the strong dipole field of Earth is responsible for its successful atmospheric retention and hospitable environment. However, this assumption has been challenged by recent observations. Several spacecraft have been able to measure heavy ion escape from Earth's atmosphere, yielding escape rates on the order of 10^{24} s^{-1} under solar minimum conditions [14]. Earth's strongly magnetized nature provides the expectation that ion escape rates should be lower than at planets that are non-magnetized, such as Mars and Venus, but this is not consistent with atmospheric observations.

Because Mars is an unmagnetized planet, it is less protected from the incoming solar wind, making its atmosphere potentially more vulnerable to stellar stripping, increasing ion escape rates. In 2014, the Mars Atmosphere and Volatile EvolutioN (MAVEN) mission began taking measurements of the escaping particles from the Martian upper atmosphere with the goal of analyzing the impact of atmospheric escape on the evolution of the Martian climate [10]. Through MAVEN and Mars Express (MEX) observations, the heavy ion escape rates are estimated to be on the order of 10^{24} s^{-1}, just like Earth's heavy ion escape rates [4, 6, 15].

The same expectations can be made for Venus due to its non-magnetized nature. Venus Express (VEX) arrived at Venus in 2006 to investigate the Venusian atmosphere with an Ion Mass Analyzer (IMA) onboard to measure the ion fluxes [14]. Barabash et al. (2007) and Persson et al. (2018) used VEX measurements to produce the recent heavy ion escape rate also on the order of 10^{24} s^{-1}, matching the estimates from Earth and Mars [1, 13].

Because observational data confirms that heavy ion escape rates are on the same order of magnitude across three planets with different dipole field strengths, ion loss depends on several other factors than just intrinsic dipole field strength alone. A different approach to studying planetary ion loss is needed to determine concise scaling laws for atmospheric ion escape.

Modeling has been a common approach in understanding the atmospheric loss processes of terrestrial planets. For the purposes of this project, we look at the modeling results of a Mars-like planet with emphasis on different parameters, such as dipole field strengths that correspond to weak magnetization and stellar parameters that might influence atmospheric escape, such as IMF orientation. Egan et al. (2019) used a hybrid plasma model to analyze the impact of intrinsic dipole field strength in the weakly magnetized realm to determine its effects on ion escape rates, finding that heavy ion escape peaks at an intrinsic dipole field strength of 50 nT with an IMF that is roughly perpendicular to the planetary dipole field [9]. Ma et al. (2004) used a fully magnetohydrodynamic (MHD) model to simulate solar wind interactions with Mars at solar minimum and maximum, replicating previous observational results [12]. Sakai et al. (2018) also used a fully MHD model to compare heavy ion escape rates between non-magnetized and weakly magnetized (100 nT) Mars-like planets [18]. In this study, ion escape rates increase with the introduction of an intrinsic dipole field with the IMF oriented roughly perpendicular to the dipole field axis [18]. Following this study, Sakai et al. (2021) used the same MHD model to determine the IMF orientation dependence on atmospheric escape from a weakly magnetized planet by manipulating the north-south component of the IMF [16]. Sakai et al. (2023) replicated their previous while incorporating a comparison of unmagnetized and magnetized planetary initial conditions. IMF orientations parallel to the dipole field (northward) results in lower escape rates, while antiparallel IMF (southward) increases ion escape rates [17].

1.4 Path Forward

Based on previous studies, we investigate the effects of intrinsic dipole field strength and IMF orientation on O^+ and O_2^+ escape from a weakly magnetized, Mars-like planet through modeling. Modeling ion escape from a weakly magnetized planet requires a global plasma model that approximates the trajectories of planetary and solar wind ions during magnetic field interactions between the planetary dipole field and the IMF. There are several model types that can simulate these plasma interactions, such as kinetic, single-particle models and MHD, two-fluid models. A kinetic model tracks individual particle motion and charge separations but can be extremely computationally expensive given the particle number densities of the solar wind particles and planetary ions. MHD models take a fluid approach, approximating the ions and electrons as continuous fluids where the fluid flow can be easily manipulated by magnetic fields. While this is a model that is beneficial for allocating computational resources due to the lack of single-particle tracking, it is not the best for approximating how individual species interact with the embedded magnetic fields in the planetary environment. The optimal choice is to combine these two plasma models into a hybrid model to accurately and efficiently model plasma interactions near the planet.

Here, we look at three separate intrinsic dipole field strengths, 0 nT, 50 nT, and 100 nT, while varying the IMF direction that is broken up into clock angle and cone angle. To do this, we will be using a 3D global hybrid plasma model (discussed in detail in Chapter 3). Using this hybrid model, we describe the methods used in this study and describe the initial conditions and parameters explored, such as dipole field strengths and IMF orientations in Chapter 2. In Chapter 3, we present results for one dipole field strength and IMF orientation to give us a 'base case' for means of comparison through the study. In Chapter 4, we present results for IMF clock angle dependence on ion escape. In Chapter 5, we present results for IMF cone angle dependence on ion escape. In Chapter 6, we present results for intrinsic dipole field strength on ion escape rates for each IMF orientation. Chapter 7 summarizes the results and highlights our conclusions.

Chapter 2

Methods

To determine the effect of magnetic fields on atmospheric loss, we use RHyrbid, a 3D global hybrid plasma model developed at the Finnish Meteorological Institute [11]. This model, paired with high performance computing, is used to simulate planetary ion escape from a weakly magnetized, Mars-like planet. RHybrid combines MHD and kinetic theory by approximating planetary ions as macroparticles with the same mass, charge, and velocity while the electrons are approximated as a charge-neutralizing, continuous fluid. This allows for computational efficiency as compared to a fully kinetic model while representing ion motion and increased physical accuracy as compared to a pure MHD model.

2.1 Model Specifications and Analysis

The results from RHybrid are in Planet Stellar-Orbital (PSO) coordinates, which take the Mars-like planet at the origin of the coordinate system. The x-axis is defined to be the planet-stellar line, pointing towards the star through the upstream region of the solar wind. The z-axis is defined to be perpendicular to the orbital plane, pointing straight through the rotational axis of the planet. The y-axis then completes the right-handed coordinate system, defined in the orbital plane of the planet. Each simulation results in a 120x120x120 grid that spans 10 planet radii (R_p = 3390 km = 1 Martian radius), ranging from -6R_p to -4R_p in the x direction with the planet at the origin, and $\pm 5R_p$ in the y and z directions.

The hybrid model used here tracks three ions through the simulation: H^+, O^+, and

O_2^+. RHybrid calculates ion velocities, densities, and escape rates in each spatial block within the simulation, which corresponds to 282.5 km per block. Each simulation was run to dt = 123,500 with $\Delta t = 0.01$ s (more than satisfying the Courant condition), except for two simulations for the magnetized case, which were run to dt = 99,000 due to computational resource restrictions.

The planet in the simulation is approximated as a conducting sphere, allowing for induced magnetospheres to form when the planet is unmagnetized. When magnetized, the dipole field strength is implemented on the surface of the planet at the equator.

Data visualization of the simulation results were created using Analysator, a data visualization package developed by the Finnish Meterological Institute [2].

Table 2.1: RHybrid upstream conditions, where $|B_{IMF}|$ is the magnitude of the IMF, v_{sw} is the velocity of the solar wind, u_{sw} is the solar wind density, and T_{sw} is the temperature of the solar wind.

Upstream Conditions	
u_{sw}	$[-351.1,\ 0,\ 0]$ km s^{-1}
n_{sw}	4.85 cm^{-3}
T_{sw}	$59,150$ K
$\lvert B_{IMF}\rvert$	5.59 nT

Initial conditions within the simulation are set, such as solar wind conditions and the ion production rates, injection locations, and corresponding temperatures. Solar wind upstream conditions and ion production initial conditions are given in Table 2.1 and Table 2.2 respectively.

The planetary dipole field strength is varied across three strengths, 0 nT, 50 nT, and 100 nT, ranging from non-magnetized to magnetized. In a previous study, ion escape rates are highest with an intrinsic dipole field strength of 50 nT and lowest at 0 nT with an IMF orientation that is roughly perpendicular to the dipole field axis [9]. This project will explore how these escape rates change with varying IMF orientations to determine if the magnitudes of escape are the same with the respective dipole field strengths.

Table 2.2: RHybrid ionospheric and exopspheric boundary conditions, where R_{em} is emission radius, R_{exo} is the radius of the exosphere, P_{iono} , P_{exo} , T_{iono}, and T_{exo} are the are the production rates and temperatures at the ionosphere and exosphere respectively.

	Ionosphere			**Exosphere**	
Parameter	O^+	O_2^+	**Parameter**	O^+	H^+
R_{em}	300 km	300 km	R_{exo}	300 km	300 km
P_{iono}	1.4×10^{25} s^{-1}	2.0×10^{25} s^{-1}	P_{exo}	1.6×10^{23} s^{-1}	2.2×10^{24} s^{-1}
T_{iono}	$20,000$ K	$20,000$ K	T_{exo}	$6,500$ K	$6,500$ K

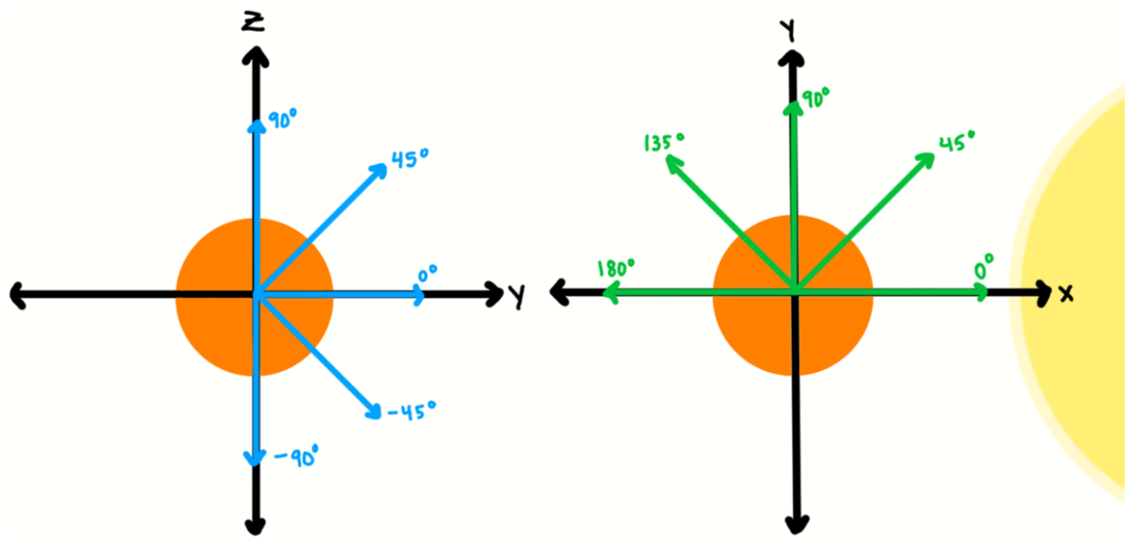

Figure 2.1: Schematic illustration of the clock and cone angle definitions. Clock angle (left) is defined to be in the terminator plane and cone angle (right) is defined to be in the orbital plane of the planet.

The dependence of IMF clock angle (ϕ) and cone angle (θ) on ion escape rates are explored in this project. Clock angle is defined in the y-z plane, or the terminator plane, with a range from 90° (pointing along the positive z-axis) to -90° (pointing along the negative z axis). Cone angle is defined in the x-y plane, or in the orbital plane of the planet, with a range from 0° (pointing along the x axis, directly towards the star) to 180° (pointing directly towards the planet), shown in Figure 2.1.

To explore the clock angle dependence on planetary ion escape rates, a clock angle of 0° is isolated, which is perpendicular to the planetary dipole axis and points along the positive y axis, while all cone angles (0° to 180°) are explored. This clock angle was chosen as it is the most neutral state due to its orientation not being parallel or anti-parallel to the planetary dipole field, corresponding to a closed and open magnetosphere respectively. A complete table of dipole field strengths and IMF orientations is shown in Table 2.3.

Table 2.3: List of 23 simulations with three dipole field strengths and IMF orientations in terms of clock and cone angles. Three orientations listed are redundant due to their overlap between IMF clock and cone angle exploration.

Dipole Field Strength	ϕ Clock Angle	θ Cone Angle
0 nT	0°	0°, 90°, 180°
50 nT	0°	0°, 45°, 90°, 135°, 180°
100 nT	0°	0°, 45°, 90°, 135°, 180°
0 nT	$-90°$,0°, 90°	90°
50 nT	$-90°$, $-45°$,0°,45°, 90°	90°
100 nT	$-90°$, $-45°$,0°,45°, 90°	90°

2.2 Simulation Convergence

When calculating the escape rates of planetary ions, we verify that each simulation has converged. In RHybrid, ion escape rates are automatically calculated by counting the number of charged particles leaving the outer boundary of the simulation domain. However, these rates are only reliable if the simulation has reached a steady state and is not evolving in time. For example, charged particles in the low energy magnetotail region can take long periods of time to reach the outer boundary of the simulation space, making the escape rates inaccurate unless the simulation is run for sufficiently long periods of time. This can be computationally expensive and impractical.

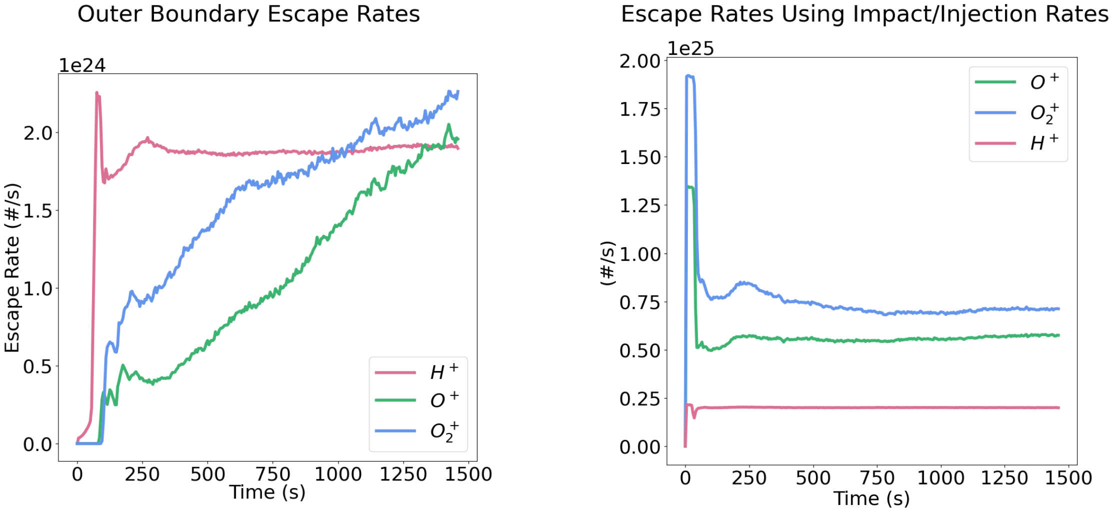

Figure 2.2: A comparison of escape rates calculated by RHybrid on the outer boundary of the simulation (left) and escape rates using the Impact and Injection rates (right). H^+ (pink) remains constant in each plot, while O^+ (green) and O_2^+ (blue) escape rates are not converged on the boundary, but they are using the adjusted calculations, shown by the linearity of the curves.

To mitigate this, I instead compute the escape rates based on information from the inner boundary of the simulation space by using the impact and injection rates of each ion species. The impact rate is the rate at which ions hit the inner boundary near the planet and the injection rate is the rate at which ions are produced within the simulation. Because of this, a reasonable and stable estimate for ion escape rates is calculated by subtracting the impact rate from the injection rate. The impact rate is the rate at which particles hit the inner boundary of the planet, which is defined to be 100 km above the surface. The injection rate is the rate at which different ion species (H^+, O^+, and O_2^+) are injected into the simulation. The escape rates derived from the impact and injection rates are averaged over the last 4 minutes of simulation time, corresponding to 24,000 time steps, which is where the escape rates converge.

This calculation determines how many particles are within the simulation domain and assumes that all particles injected into the simulation will eventually escape on the outer boundary. This method is computationally efficient since the environment near the inner boundary stabilizes at a much higher rate than the outer boundary. When the simulation is in a steady state, the escape rates calculated using the impact and injection rates and the escape rates on the outer boundary calculated by RHybrid will be about the same.

Chapter 3

The Base Case

Here we describe simulation results for one intrinsic planetary dipole field strength and IMF orientation, which we refer to as the “base case”. These results will be used in comparison to other field strengths and IMF orientations later in this project. The base case is defined to be when the intrinsic dipole field strength is 100 nT with an IMF orientation defined by a clock angle of 0° and a cone angle of 90°. This was chosen to be the base case as the planet has a natural magnetosphere as well as an induced magnetosphere that occurs for all explored dipole field strengths. This IMF orientation was chosen because it is the shared orientation between the clock angle and cone angle exploration spaces.

Plasma Boundaries As the upstream solar wind travels towards the planet, it impacts the bow shock that overlaps with the magnetopause, which is the region where the solar wind slows down as it comes into contact with the planetary magnetosphere. The slowing of the solar wind and the region of the bow shock is best described when looking at the velocities of the upstream solar wind, as shown in Figure 3.1. The upstream solar wind impacts the bow shock with a velocity of 351.1 kms^{-1}, as defined in Chapter 2, and slows down as it enters the magnetosphere and diverts around the planet. The IMF that is embedded within the solar wind drapes around the planetary magnetosphere, explaining the magnetospheric boundary seen in Figure 3.2. This is a boundary that is observed later in the Chapter 4 and Chapter 5 when exploring clock angle and cone angle dependence respectively.

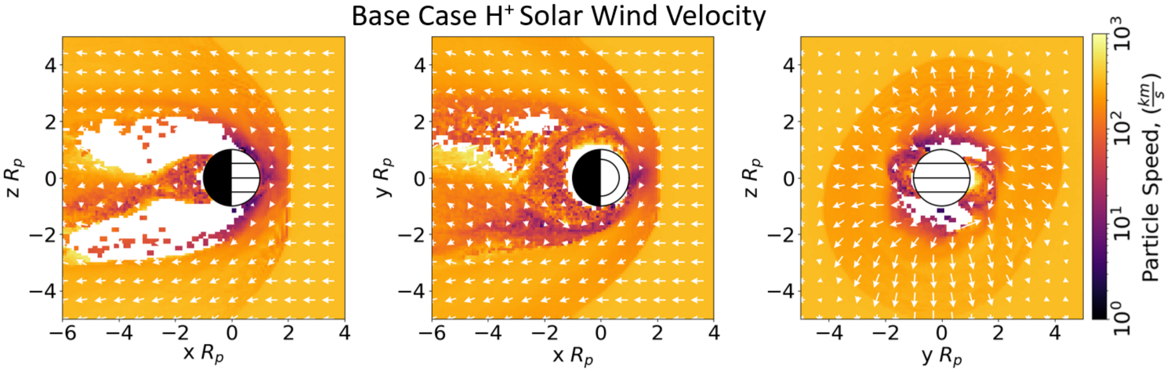

Figure 3.1: Plots of the solar wind velocity through the simulation domain. The colormap is the magnitude of the solar wind velocity and the white quivers show the magnitude and direction of the solar wind in each 2D spatial slice.

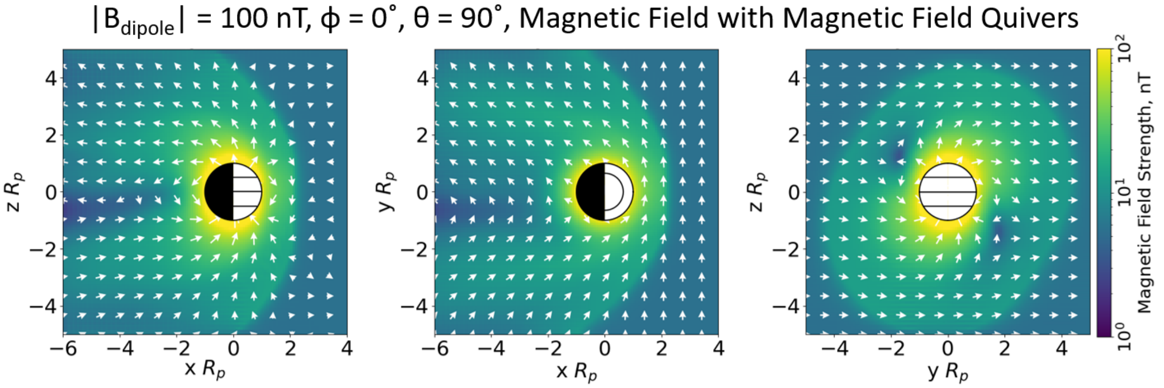

Figure 3.2: Plots of the magnetic field structure of the base case, intrinsic dipole field strength of 100 nT and an IMF orientation of clock angle 0° and cone angle 90°. The magnetosphere's structure is shown by white magnetic field quivers with the magnitude of the magnetic field as the colormap in three 2D spatial planes.

Magnetospheric Configuration In the xz plane, the magnetospheric configuration is closed on the dayside and nightside of the planet with open magnetic field lines extending out of the polar regions. The magnetosphere has an axial tilt off of the geographic axis because the IMF is directed entirely in the +y direction. This axial twisting is best seen in the yz plane (rightmost panel of Figure 3.2), also showing magnetic null points on either side of the planet. These null points are due to the orientational difference between the planetary dipole field lines and the IMF which cancels out the field, leaving a high probability of magnetic reconnection points in these regions.

Ion Loss Cloud Morphologies Though they are overall similar, there are some key differences between the fluxes of O^+ and O_2^+ shown by the ion loss clouds. The structural differences in the ion clouds, such as how 'diffuse' the clouds are, or why O_2^+ has a more spread out ion cloud as compared to O^+, can be attributed to the mass difference between the ions. Because O_2^+ has a larger mass, it has a larger gyroradius, accounting for a larger ion loss cloud and a larger arc for the dayside plume. The ion plumes are due to the convection electric field that points along the +z-axis and is analyzed in Chapter 5.

The velocities are lower in the low-energy magnetotail region, as shown by the shorter quiver lengths in Figure 3.3. This is because in this configuration, the ions are being trapped in this region of the magnetotail, supported by the closed magnetospheric configuration shown in Figure 3.2. This pattern is consistent with both planetary ion species. The ion acceleration along the +z-axis, shown in the xz and yz planes of Figure 3.3 can be attributed to the Lorentz force, which allows the ions to be accelerated by the convection electric field along the +z-axis.

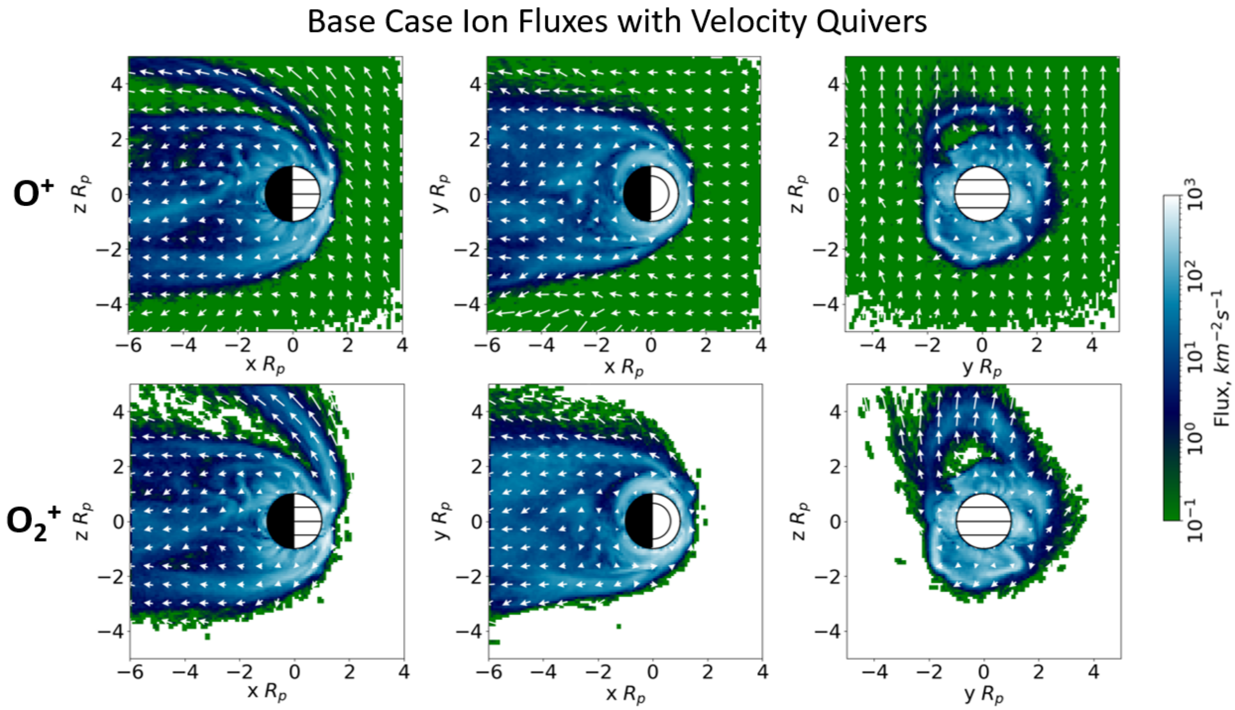

Figure 3.3: Plots of the the O$^+$ (top) and O$_2^+$ (bottom) fluxes in three 2D spatial slices. The colormap represents the ion fluxes with velocity quivers plotted over top for the respective species.

Table 3.1: Ion escape rates for the base case.

Base Case Escape Rates	
O^{+}_{esc}	$8.33 \times 10^{24}\ s^{-1}$
$O^{+}_{2\ esc}$	1.28×10^{25} s^{-1}

Ion Escape Rates for the Base Case The escape rates of O$^+$ and O$_2^+$ shown in Table 3.1 and are calculated using the injection and impact rates, as explain in Chapter 2. The base case heavy ion escape rates are the same order of magnitude of those observed by MAVEN and MEX [4, 6, 15]. These escape rates will be the basis of comparison for the subsequent ion escape rate calculations for other dipole field strengths and IMF configurations. All further analysis on clock and cone angle dependence on ion escape rates will be using a 100 nT dipole field strength to see how the base case is affected by IMF orientation.

Chapter 4

Clock Angle Dependence on Ion Escape

Here, we explore the role of IMF clock angle on magnetospheric morphology and ion escape rates. Building off of the base case, an IMF cone angle of 90° is held constant while the IMF clock angle is varied -90° to 90°, which is from the negative z-axis to positive z-axis respectively.

4.1 Magnetospheric Structure and Configuration

The magnetospheric structure is shown by the white quivers in Figure 4.1. As the clock angle changes, the magnetospheric boundaries change in morphology. With a clock angle of -90°, the magnetic boundary is remarkably symmetrical and narrow, confined close to the planet. In the yz plane (right column of Figure 4.1), the magnetosphere has a symmetrical and elongated shape along the +y-axis. As the clock angle increases, the outer regions of the magnetospheric boundary widen and occupy more of the simulation domain. In the yz plane, the boundary becomes slightly more spherical and extends outside of the simulation domain when the clock angle is 90°. Asymmetries arise with an increase of clock angle as the boundary is stretched along the +y direction.

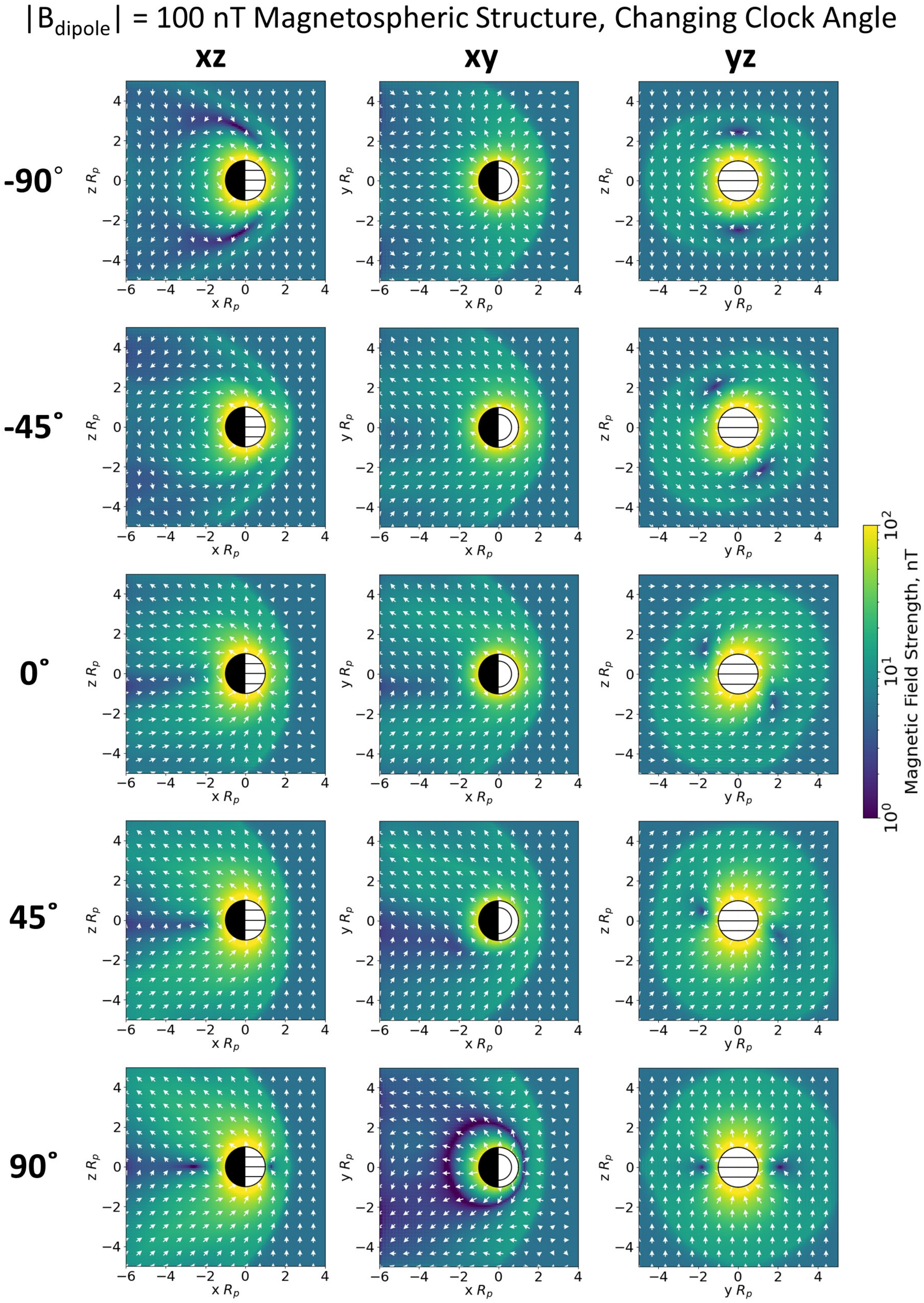

Figure 4.1: Plots showing the magnetic environments (dipole strength as a colormap and white magnetic field quivers overplotted to show magnetospheric configuration) of a 100 nT planet with a cone angle of 90° and a varying clock angle from -90° to 90° (top to bottom); visualized in all three 2D spatial slices (left to right).

The magnetospheric configuration changes with clock angle, starting with a completely closed configuration and opening up as the IMF points along the +z-axis. However, even in the open configurations (45° and 90°), there are still very few closed magnetic field lines in front of and behind the planet, though the rest of the magnetosphere is open. The purple 'null-points' in the plots represent the potential magnetic reconnection points within the magnetosphere, breaking the boundary between planetary and solar wind plasma.

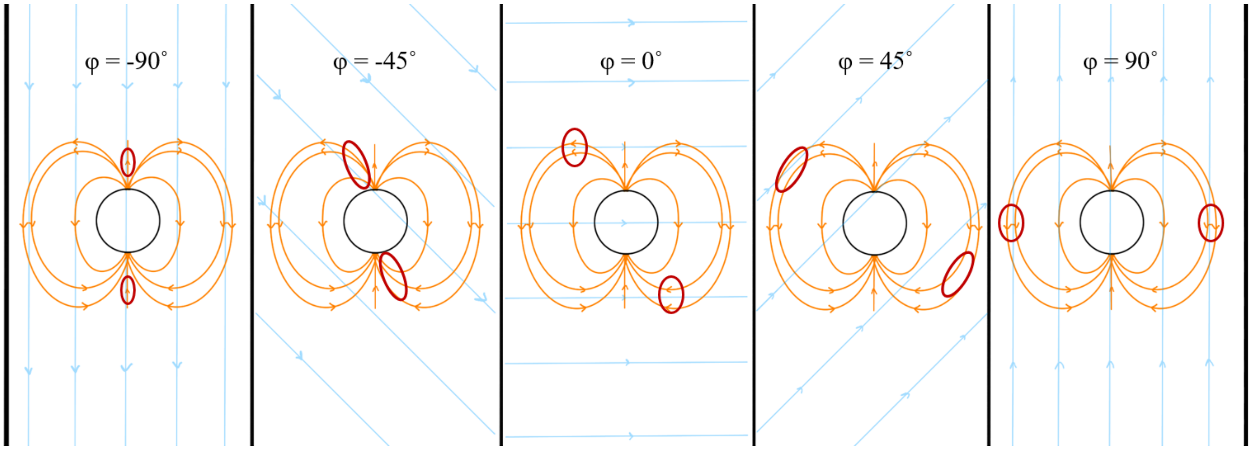

Figure 4.2: Schematic illustration showing the 90° rotation of null field points (red circle) with a change of IMF clock angle (blue lines) interacting with the planetary dipole field (orange lines).

Null Field Ring A feature in Figure 4.1 worth analyzing is the null field ring around the planet for an IMF clock angle of 90°. The null ring represents a region where the IMF cancels out the planetary dipole field. As the clock angle increases from -90° to 90°, the null ring rotates counterclockwise around the planet as seen from the position of the host star. The ring rotates a total of 90° with an IMF change of 180° because of the relative orientation between the IMF and the dipole field, as shown in Figure 4.2. Due to the opposing nature of the fields, it can be assumed that magnetic reconnection occurs at these points, but needs further flux tube analysis to confirm.

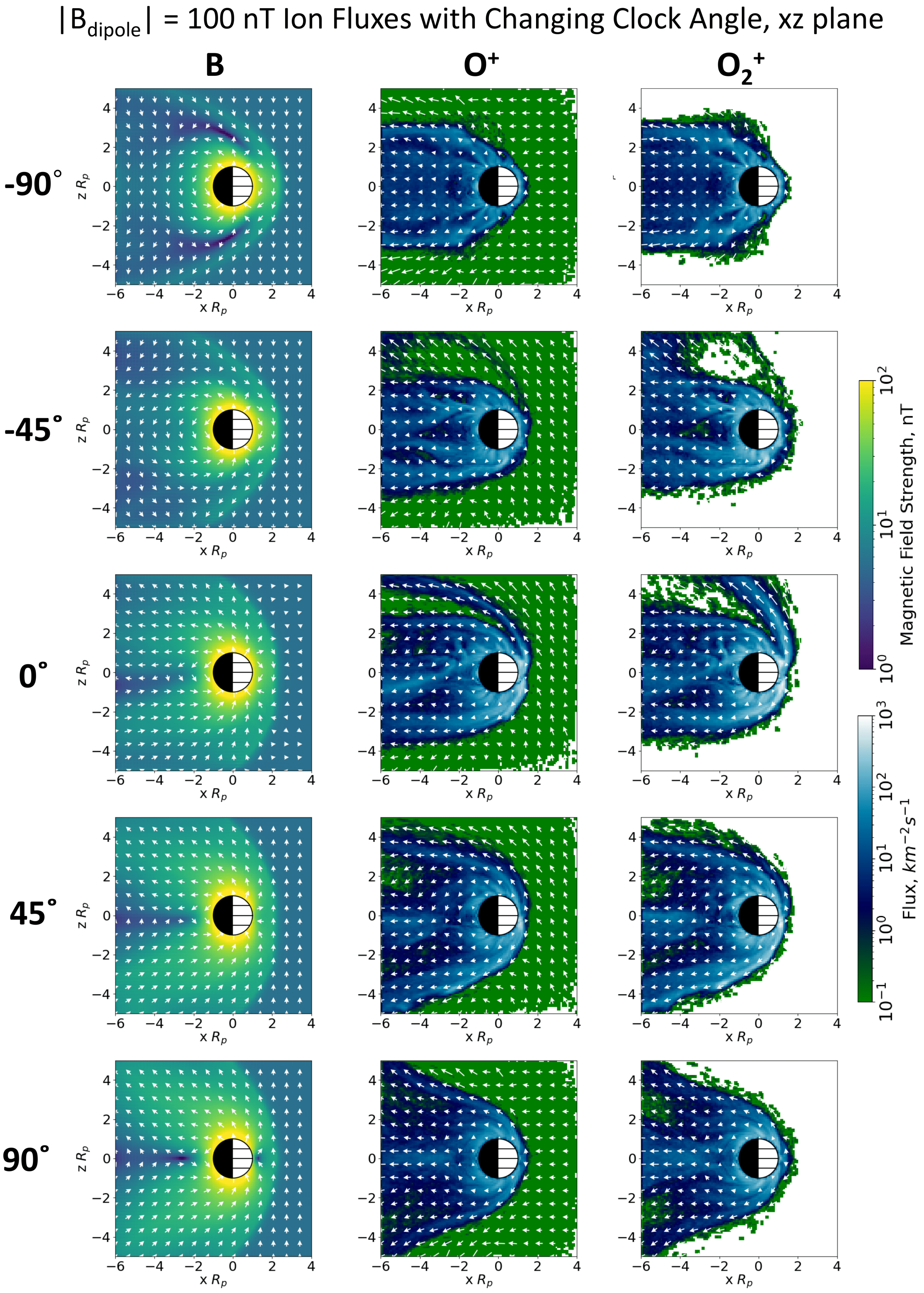

Figure 4.3: Plots showing the magnetic field with magnetic field quivers (left) and fluxes of O^+ (middle) and O_2^+ (right) with the flux magnitude as the colormap and velocity quivers plotted over top for the respective species. Shown in the xz plane.

4.2 XZ Plane Ion Cloud Morphologies and Fluxes

In Figure 4.3, the fluxes of O^+ and O_2^+ are seen farther from the planet on the dayside and span a larger spatial domain in the downstream region with an increase in IMF clock angle. This widening of the ion loss cloud corresponds to the opening of the magnetospheric configuration with increasing clock angle. This is because when the boundary between the planetary plasma and solar wind plasma is broken due to the opposing magnetic topologies, higher concentrations of the atmospheric species are able to become energized, resulting in atmospheric escape. Even as the magnetosphere opens up, there are still a few closed planetary magnetic field lines on either side of the planet, resulting in the trapping condition in the magnetotail for both species.

Corresponding to this trapping region, the ion velocities are significantly lower than in the surrounding regions, though the flux is still relatively high. This means that there is a higher density of atmospheric species in these regions of the ion clouds. The ion trajectories are dictated by the direction of the convection electric field. For example, for clock angles -45° to 45°, dayside plumes arise and flow over the northern side of the planet due to the +z component of the convection electric field.

4.3 XY Plane Ion Cloud Morphologies and Fluxes

In the xy plane, shown in Figure 4.4, the ion loss clouds are not symmetrical. At a clock angle of -90°, the ion loss clouds for both O^+ and O_2^+ have a positive y component corresponding to the direction of the solar wind convection electric field. As the clock angle increases to 90°, the ion cloud is pulled in the direction of the convection electric field as its direction changes with each clock angle adjustment. The direction of the ion loss clouds switches to being directed along the -y direction while the clouds become more diffuse, containing higher fluxes for both species.

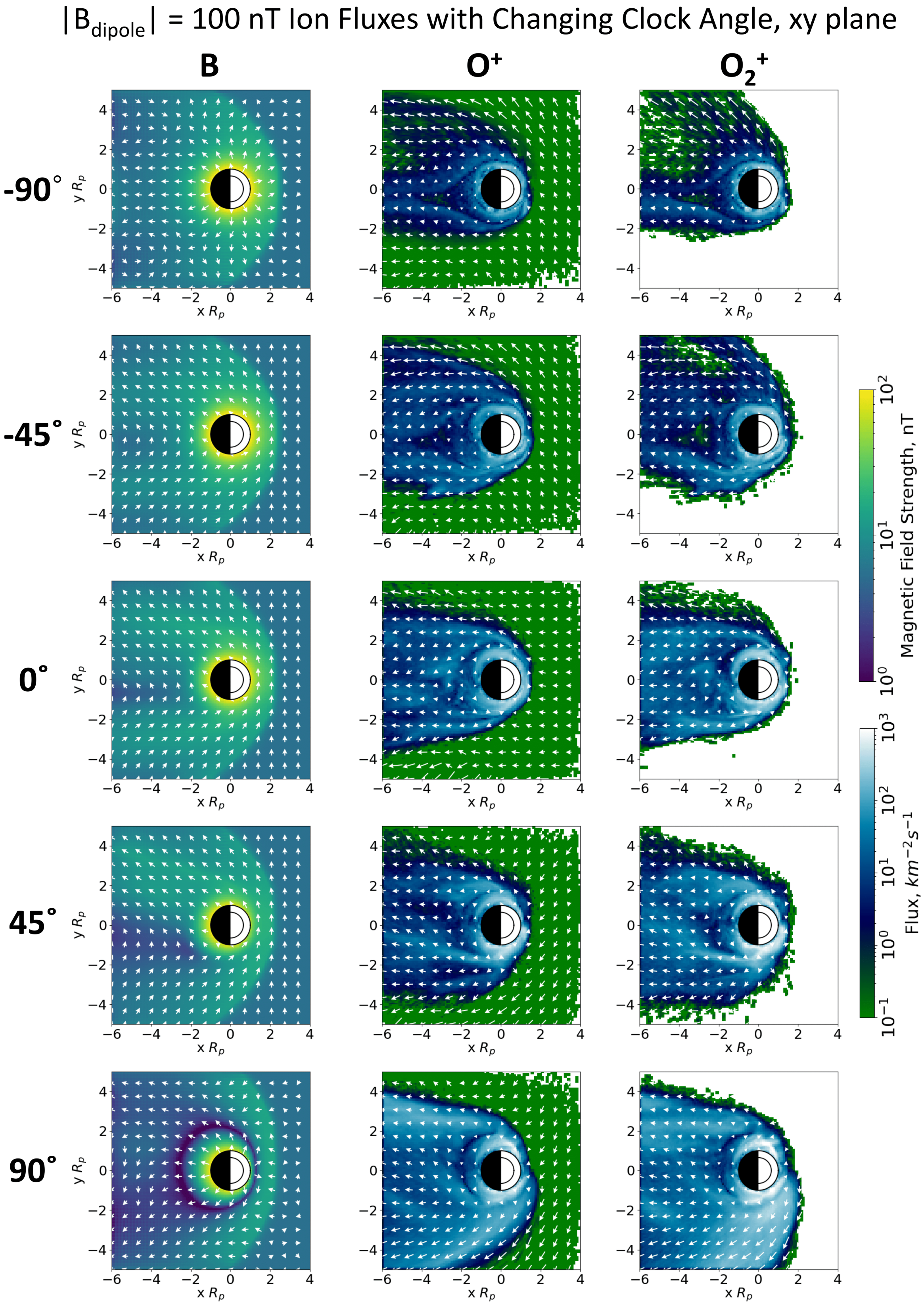

Figure 4.4: Plots showing the magnetic field with magnetic field quivers (left) and fluxes of O^+ (middle) and O_2^+ (right) with the flux magnitude as the colormap and velocity quivers plotted over top for the respective species. Shown in the xy plane.

The O^+ and O_2^+ fluxes change dramatically as the clock angle increases from -90° to 90°. In Figure 4.4, the fluxes within the ion loss clouds at a clock angle of -90° are lower due to the higher rates of magnetospheric trapping at this IMF orientation. The ion fluxes increase in magnitude within the cloud as the clock angle increases and the magnetosphere begins to open up. The increase of fluxes begins as a ring around the planet because the incoming solar wind is able to penetrate the magnetosphere and accelerate the atmospheric ions. The bright flux ring then extends throughout the cloud, showing the energized ions escaping the simulation space, best seen in the bottom row of plots in Figure 4.4 at an IMF clock angle of 90°.

4.4 YZ Plane Ion Cloud Morphologies and Fluxes

The yz plane, shown in Figure 4.5, best shows the changing clock angle and direction of the solar wind convection electric field and its influence on the direction of the O^+ and O_2^+ loss clouds. At a clock angle of -90°, the planetary ion loss clouds point along the +y axis along the convection electric field. At this IMF orientation, the ion loss clouds are concentrated close to the planet with a diffuse arc carried along the electric field. As the clock angle increases, the diffuse arc rotates to align with the +z axis, resulting in a more concentrated plume and a larger ion loss cloud around the planet. The plumes for O_2^+ are more defined and extend outside of the simulation domain for these orientations due to its larger gyroradius.

The ion loss cloud morphologies also are affected by the boundaries of the magnetosphere in each IMF configuration. For example, when the magnetosphere is closed with a clock angle of -90°, the O^+ and O_2^+ loss clouds are closer to the planet with a similar morphology to the magnetosphere: elongated along the +y direction. As the clock angle increases, the ion loss clouds continue to follow the magnetospheric configuration, becoming more spherical with only a slight elongation along the +y-axis when the clock angle if 90°, even though the convection electric field points along the -y direction.

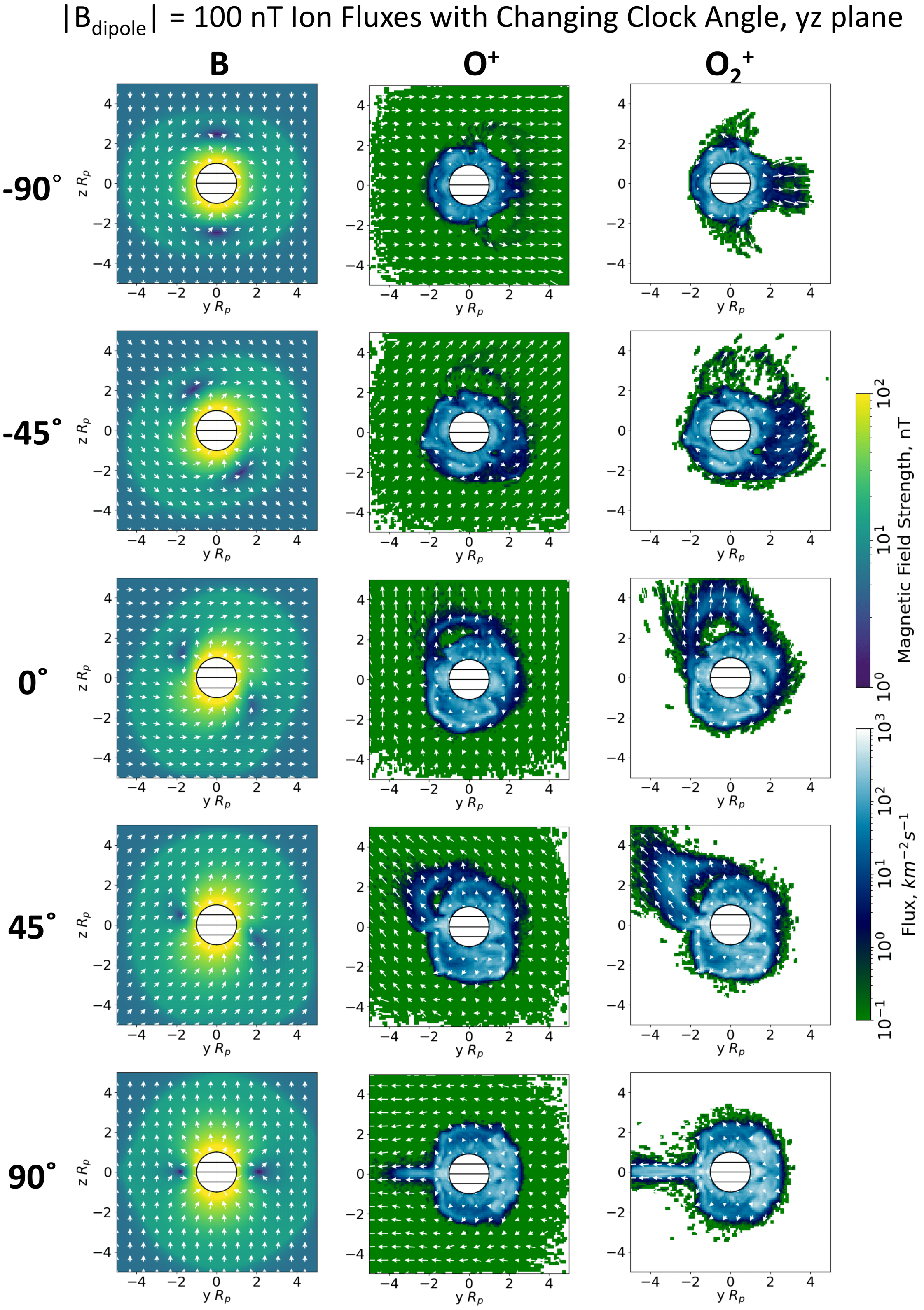

Figure 4.5: Plots showing the magnetic field with magnetic field quivers (left) and fluxes of O^+ (middle) and O_2^+ (right) with the flux magnitude as the colormap and velocity quivers plotted over top for the respective species. Shown in the yz plane.

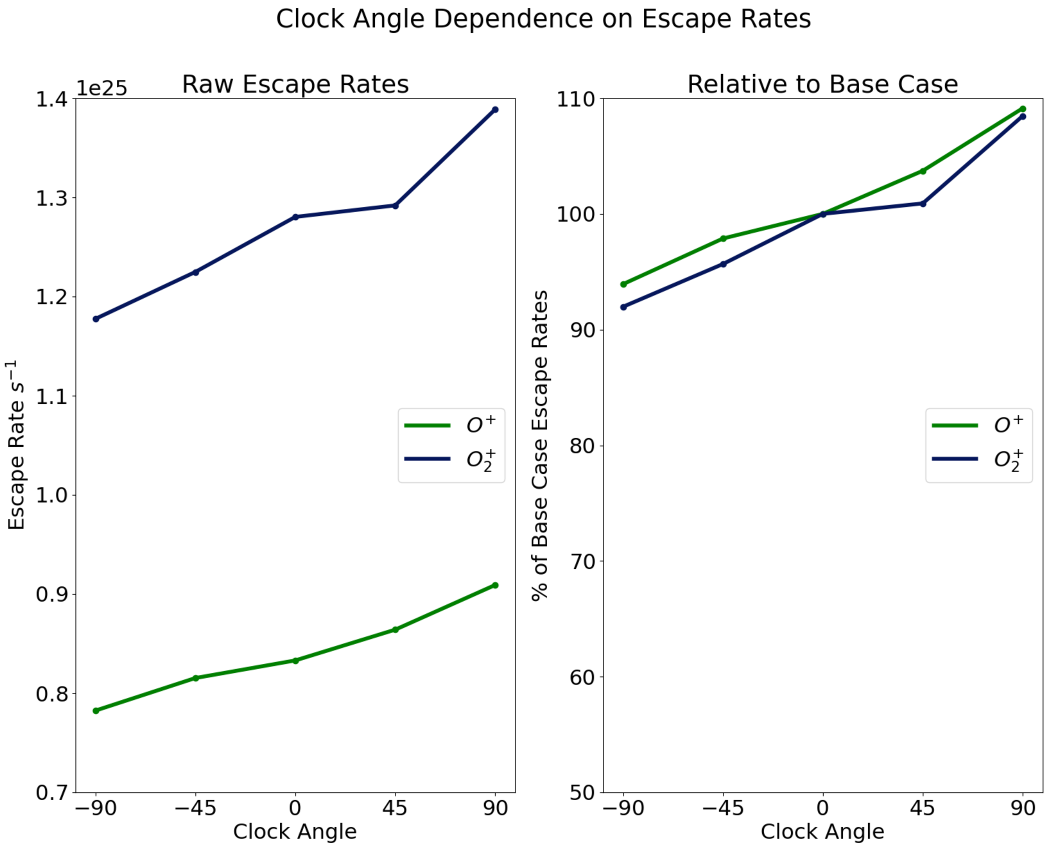

Figure 4.6: Diagram of escape rates of O^+ (green) and O_2^+ (blue) with a constant cone angle of 90° with a clock angle varied between -90° and 90°. Numerical escape rates are shown in the left panel and a comparison of escape rates to the base case are in the right panel.

4.5 Clock Angle Dependence on Escape Rates

Because the magnetosphere opens up with increasing clock angle, ion escape rates also increase with this IMF orientation change. This is seen in Figure 4.6 for both O^+ and O_2^+. IMF orientations with a dominant +z component correspond to an open magnetosphere, which leads to higher ion escape rates due to open dipole magnetic field lines. IMF orientations with a dominant -z component correspond to a closed magnetosphere, which leads to lower ion escape rates because of the abundance of closed magnetic field lines.

There is a direct correlation between open and closed magnetospheric configurations and clock angle. As the clock angle increases from -90° to 90°, more magnetic reconnection events occur, opening up the magnetosphere. The opening of the magnetosphere allows favorable conditions for atmospheric escape. This provides an explanation for the higher escape rates with an increase of clock angle.

The clock angle dependence on escape rates in this project are consistent with previous MHD modeling results, where ion escape rates are lowest with a southward IMF orientation (clock angle -90°) and higher for a northward IMF orientation (clock angle 90°) [16]. The lower ion escape rates for the northward IMF orientation are due to the closed magnetospheric configuration and the higher ion escape rates for the southward IMF orientation are attributed to the open magnetospheric configuration allowing for the IMF to penetrate into the planetary ionosphere, increasing ion loss [16].

Chapter 5

Cone Angle Dependence on Ion Escape

To explore the cone angle dependence on planetary ion loss, the base case of a planet with an intrinsic dipole field strength of 100 nT is studied with an IMF constant clock angle of 0° and a varied cone angle from 0° to 180°. The analysis follows the same course as the previous chapter.

5.1 Magnetospheric Structure and Configuration

In the xz plane, as shown in left column of Figure 5.1, there is no definite change in the magnetospheric configuration as the cone angle is varied from 0° to 180°. The magnetosphere stays closed. However, a feature to note is the null-field 'ring' for a cone angle of 0° and 180°, similar to the one seen in Chapter 4. The cancellation of the magnetic fields is shown in Figure 5.2 showing a superposition of the planetary dipole field and the IMF, as well as the likely points of reconnection, corresponding to the null-field ring.

5.1.1 Null Field Regions

We consider why the null field ring is present in the cases where the IMF is aligned with the x-axis (planet-stellar line). Close to the planet, where the dipole field is strongest, there is a null-field point on the day side of the planet, roughly two planetary radii away from the surface. In this region, we can expect reconnection to occur rather than the fields canceling out due to the high strength of the dipole field in this region.

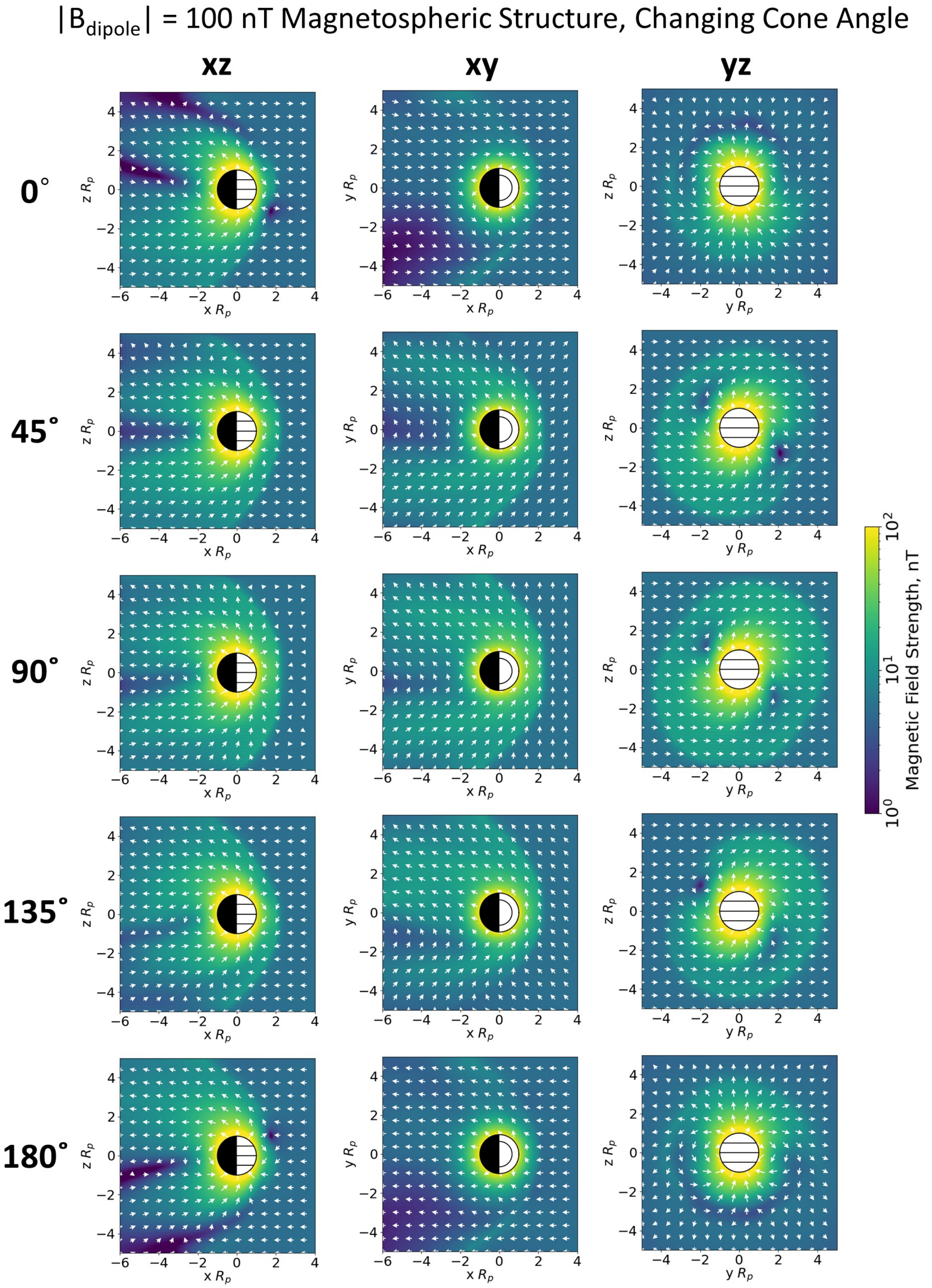

Figure 5.1: Plots showing the magnetic environments (dipole strength as a colormap and white magnetic field quivers overplotted to show magnetospheric configuration) of a 100 nT planet with a clock angle of 0° and a varying cone angle from 0° to 180° (top to bottom); visualized in the all 2D spatial slices.

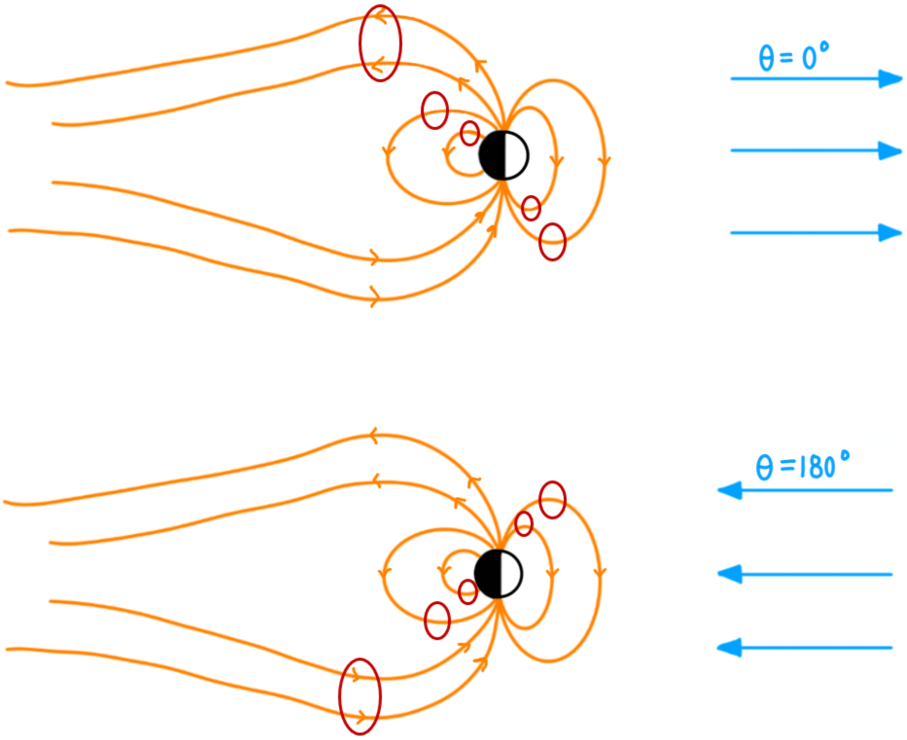

Figure 5.2: Schematic diagram of the planetary dipole field (orange) and IMF (blue) for a clock angle of 0° and cone angles of 0° (top) and 180° (bottom) with the null-field regions indicated with red circle for the xz plane.

However, far away from the planet, where the null-field ring occurs on the nightside, it is more likely that the IMF and dipole fields cancel each other out because the planet's dipole field strength is weaker in this region. In both cases, we cannot assume that magnetic reconnection absolutely occurs without further analysis using a different model to analyze the flux tubes in these regions.

A different view of the null field ring can be seen in the terminator plane (yz plane), shown in the right column of Figure 5.1. The null field points are oriented in the same configuration as the ones in the base case, but for cone angles 45°, 90°, and 135°, the relative strength of the null points vary. The location of the null points stays the same due to the constant clock angle of 0°, but the strength of the null points varies due to the rotation in the null field ring shown in the yz plane. Along with this, there is a faint null ring for cone angles 0° and 180° in the terminator plane, with the ring in the northern magnetosphere for a cone angle of 0° and mirrored for cone angle 180°. This is because the IMF is in the opposite direction of the planetary dipole field in these areas.

5.2 XY Plane Ion Cloud Morphologies and Fluxes

The influence of cone angle on O^+ and O_2^+ fluxes is primarily on the morphology of the ion loss clouds. In Figure 5.3, the planetary ion loss clouds are symmetric about the base case orientation: IMF clock angle 0° and cone angle 90°. This symmetry is reflected over the y axis and can be attributed to the strength of the convection electric field. The upstream electric field vanishes with a cone angle of 0° and 180° because the IMF and the velocity of the incoming solar wind are antiparallel and parallel respectively. The O^+ and O_2^+ ion clouds in these configurations, as shown in the top and bottom rows in Figure 5.3, have the most diffuse clouds with high ion fluxes on the dayside of the planet, outside of the magnetospheric boundary. Inside of the magnetospheric boundary, ions are accelerated along the dipole electric field.

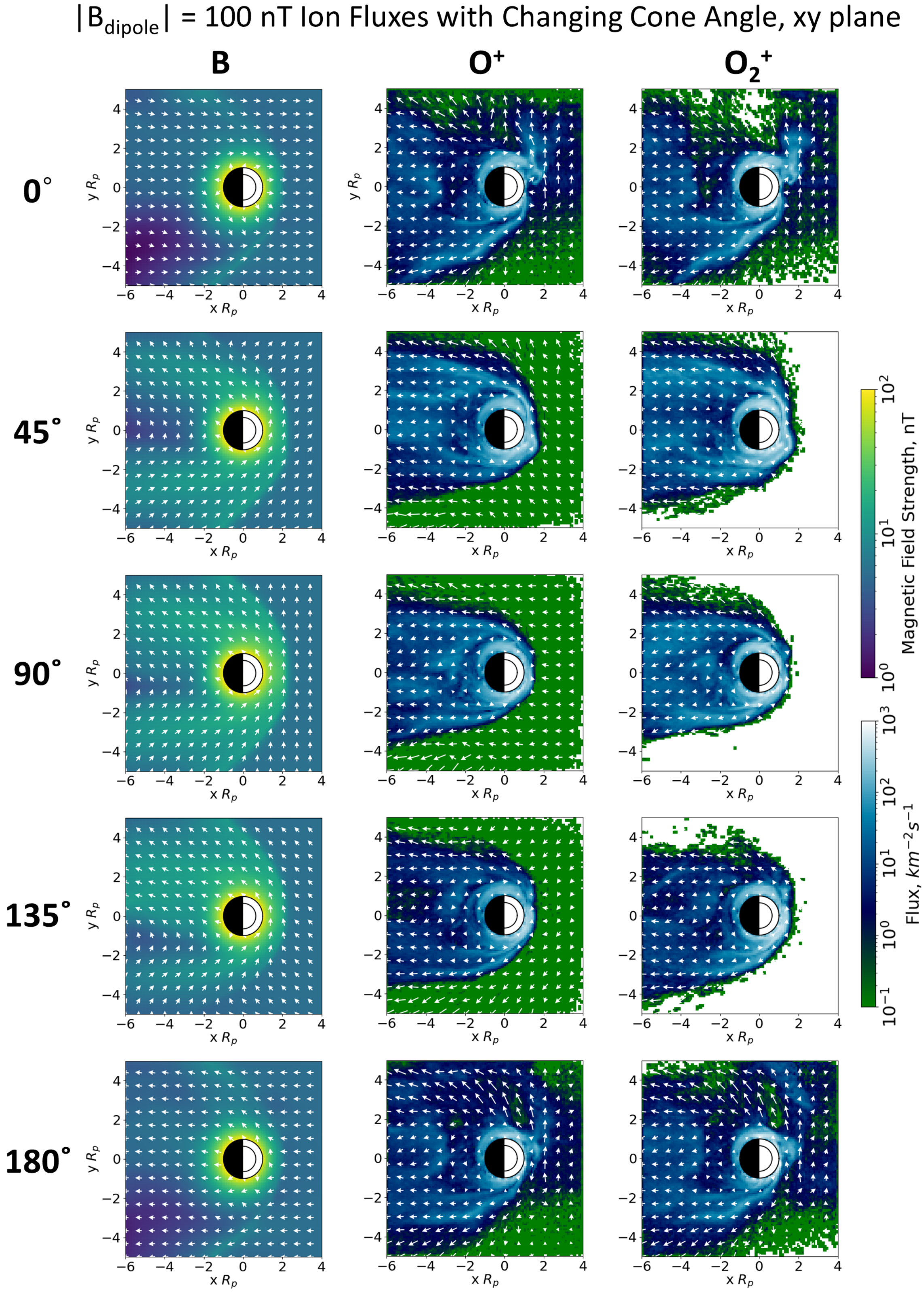

Figure 5.3: Plots showing the magnetospheric configuration (left), fluxes of O^+ (middle) and O_2^+ (right) in the xy plane through all cone angles.

The convection electric field becomes nonzero for the other cone angles (45°, 90°, and 135°). In these IMF configurations, the ion clouds are contained by the magnetosphere on the dayside and are heavily influenced by the IMF convection electric field. For cone angles 45° and 135°, the electric field is the same magnitude but in opposite directions (45° points between +y and +z, 135° points between -y and +z). For a cone angle of 90°, the ions accelerate along the convection electric field that aligns with the +z direction. The ion trajectories are best seen in the terminator plane in Figure 5.4.

5.3 YZ Plane Ion Cloud Morphologies and Fluxes

In the yz plane (Figure 5.4), the effect of the null field points on the ion cloud morphology is shown with varying degrees of cone angle. Just as in xy plane, symmetry exists along the y axis, but also along the z axis. Cone angles 45°, 90°, and 135° are similar in morphology with respect to the z axis, but there is complete asymmetry for the configurations where the convection electric field is zero. Though the ion morphology patterns are symmetric around a cone angle of 90°, it is important to note the ion cloud asymmetries within each configuration. For IMF orientations where the convection electric field is non-zero, the ion loss clouds point mainly along the +z-axis. However, for the cases of radial IMF (cone angles 0° and 180°), the ion loss clouds are dragged along the +y axis.

As for the cases where the solar wind convection electric field is zero, the planetary dipole field dictates the motion of the ions and their escape, as shown in the top and bottom rows of plots in Figure 5.4. The ions are ejected along the +y axis and gyrate around the planet due to the dipole-generated convection electric field, driving the atmospheric escape in these cases.

Also in Figures 5.1 and 5.2, there are high density rings of O^+ and O_2^+ around the planet where the species are injected into the simulation. This is because for the constant clock angle of 0°, the magnetospheric configuration is closed and does not change drastically with cone angle variation. The magnetosphere traps the O^+ and O_2^+ in these regions and

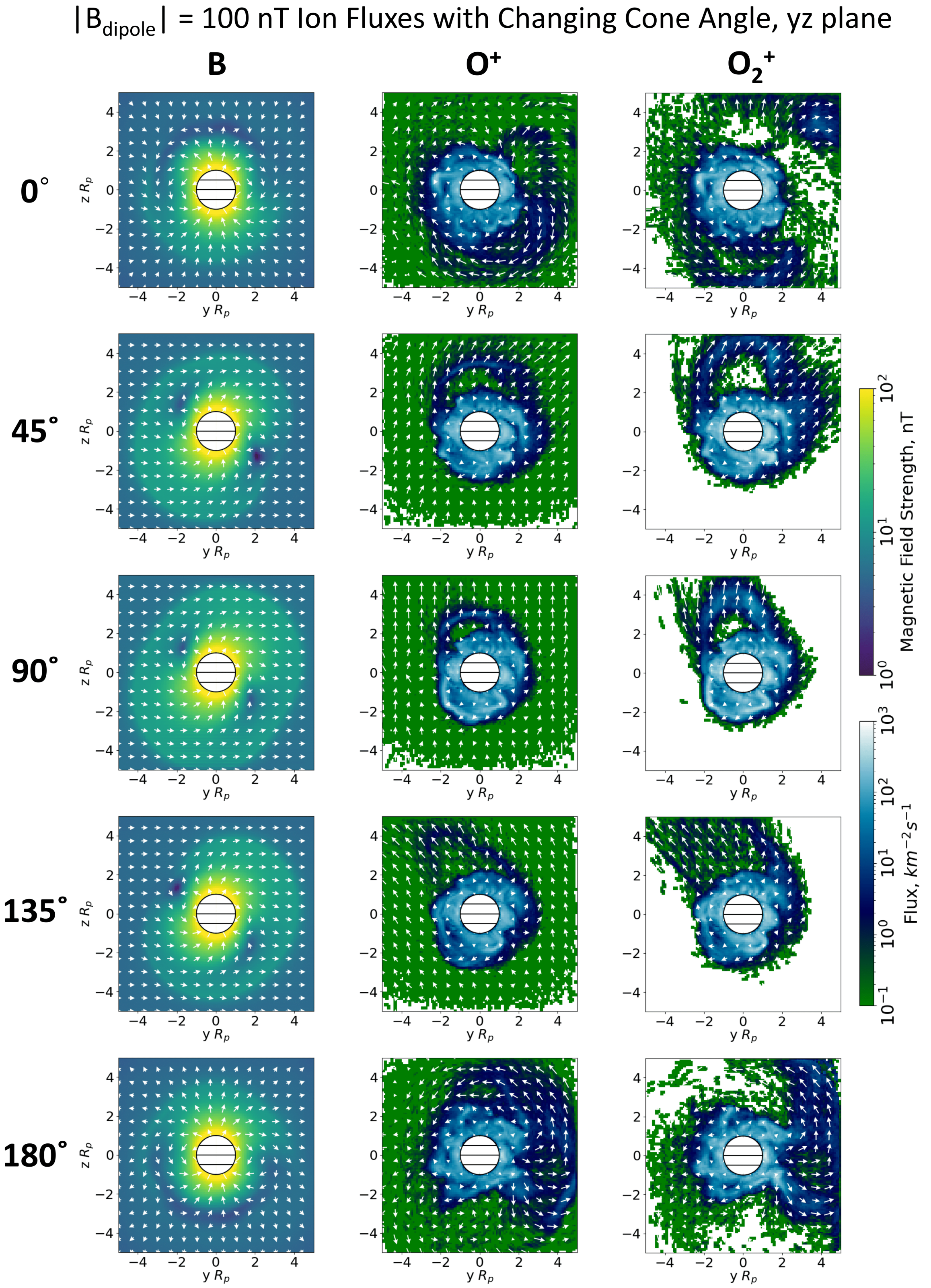

Figure 5.4: Plots showing the magnetospheric configuration (left), fluxes of O$^+$ (middle) and O$_2^+$ (right) in the yz plane through all cone angles.

they gyrate around the closed field lines close to the planet.

5.4 XZ Plane Ion Cloud Morphologies and Fluxes

In the xz plane (Figure 5.5), ion plumes can be seen stretching over the northern side of the planet for cone angles 45°, 90°, and 135°. However, the densities and velocities of the plume change with the strength of the electric field, strongest at cone angle 90° and weaker at cone angles 45° and 135°. Because the electric field is strongest with a cone angle of 90°, the plume ions have higher velocities and more easily escape. The plumes originate on the dayside of the planet around the subsolar point. The O_2^+ plume extends farther out into the dayside region than the O^+ plume due its larger gyroradius, explained previously in Chapter 4.

5.5 Cone Angle Dependence on Escape Rates

The IMF cone angle has a large effect on the atmospheric escape rates for a magnetized planet with a dipole field strength of 100 nT. There is a large variation in escape rates for O^+ and O_2^+ as the cone angle changes, corresponding to the variance in the strength and presence of the convection electric field and the resulting morphologies, such as dayside escape and subsolar plumes. The escape rates peak at IMF cone angles 45° and 135° with a slight 'dip' at a cone angle of 90°, where the electric field is strongest. The electric field in these areas accelerate the atmospheric ions to point of escape as compared to the cone angles 0° and 180°, where escape rates are lowest. This is expected due to the vanishing solar wind convection electric field when the IMF is parallel or antiparallel to the incoming wind, which is the main driver for atmospheric escape [8].

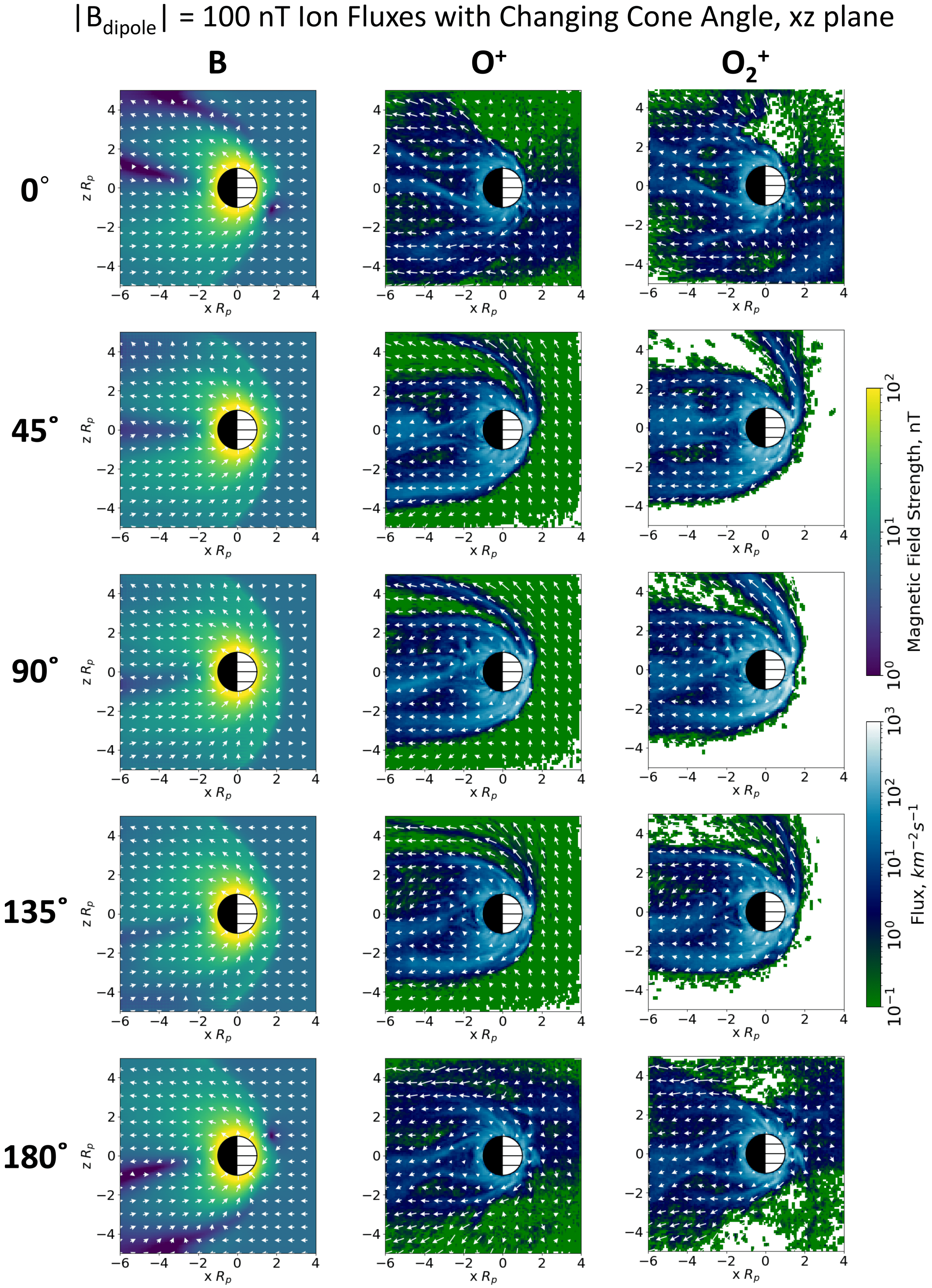

Figure 5.5: Plots showing the magnetospheric configuration (left), fluxes of O^+ (middle) and O_2^+ (right) in the xz plane through all cone angles.

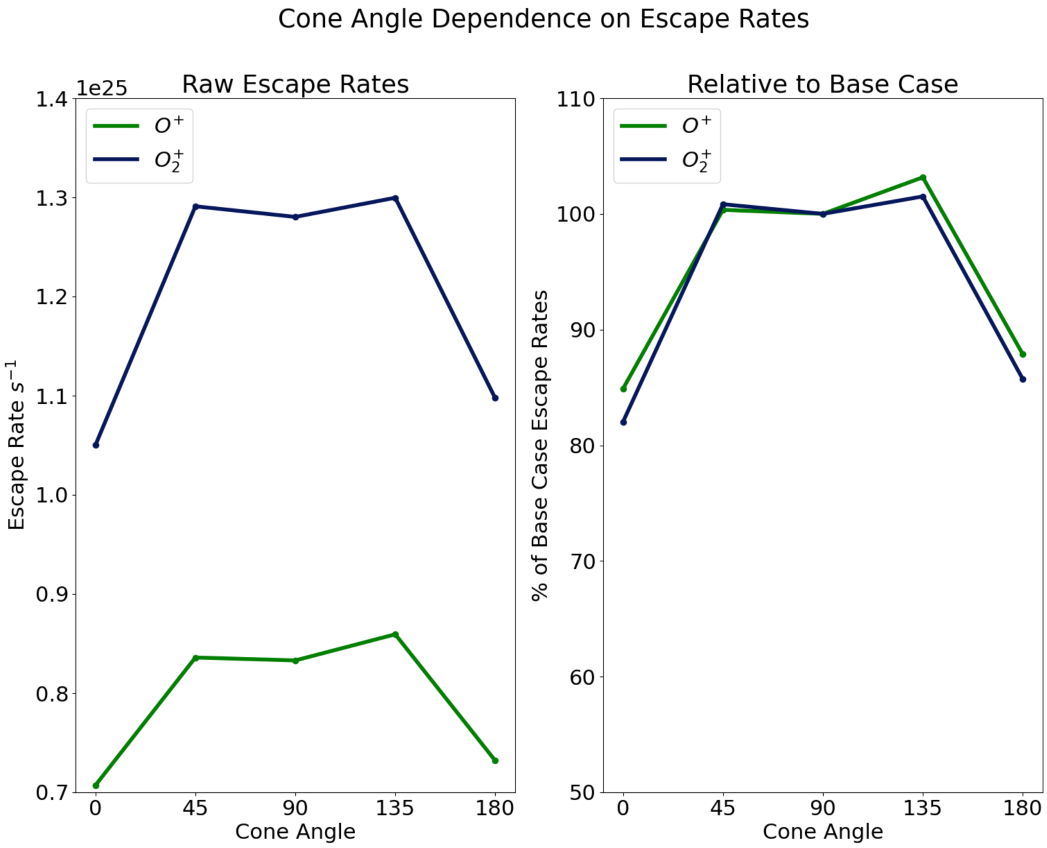

Figure 5.6: Diagram of escape rates of O^+ (green) and O_2^+ (blue) with a constant clock angle of 90° with a cone angle varied between 0° and 180°. Numerical escape rates are shown in the left panel and a comparison of escape rates to the base case are in the right panel.

Chapter 6

Planetary Dipole Field Strength Dependence on Ion Escape Rates

To explore the planetary dipole field strength dependence on ion escape rates, the previous areas of analysis (clock and cone angle dependence) are compared across three dipole field strengths: 0 nT, 50 nT, and 100 nT. These dipole field strengths range from non-magnetized to magnetized (importance discussed in Chapters 1 and 2).

6.1 Clock Angle Dependence

0 nT As the clock angle is varied from -90° to 90° with a constant cone angle of 90°, there is no trend observed for the O^+ and O_2^+ escape rates for the unmagnetized case. The O^+ escape rate is $5.61 \times 10^{24}\ s^{-1} \pm 0.5\%$ and the O_2^+ escape rate is $7.00 \times 10^{24}\ s^{-1} \pm\ 0.5\%$. The flat ion escape rate curves, as seen in Figure 6.1, are due to the lack of planetary dipole field. The only magnetosphere it obtains is when the system evolves and the solar wind particles that interact with the ionosphere produce an induced magnetosphere. There is no clock angle dependence on escape rates on the unmagnetized case because the structure of the magnetosphere is the same with clock angle variation. If a simple coordinate system transformation is performed, as shown in Figure 6.2 below, the IMF clock angle remains the same with each transformation. Because of this, the escape rates stay constant for O^+ and O_2^+, as expected.

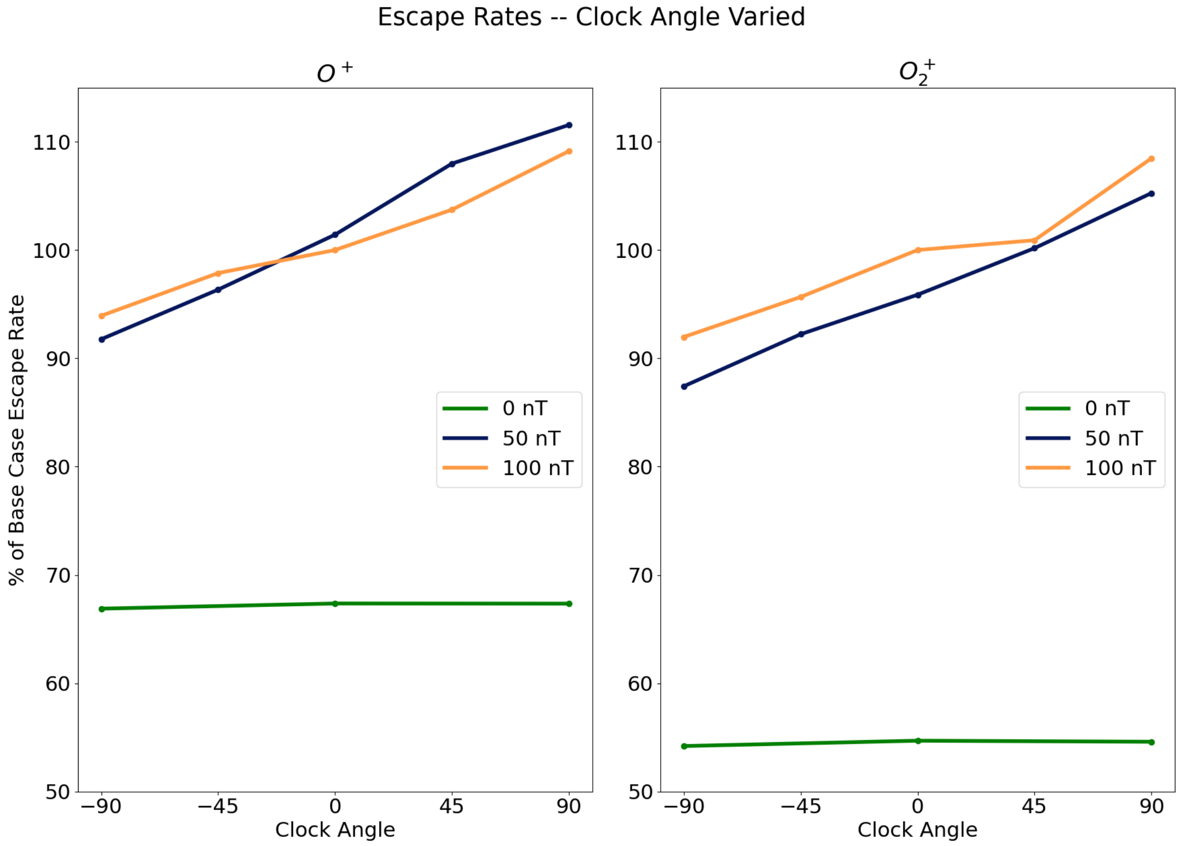

Figure 6.1: Plots comparing the 0 nT (green), 50 nT (purple), and 100 nT (orange) escape rate trends with changing clock angle for O^+ (left) and O_2^+ (right). Escape rates are presented as a percentage of the base case escape rates, defined in Chapter 3.

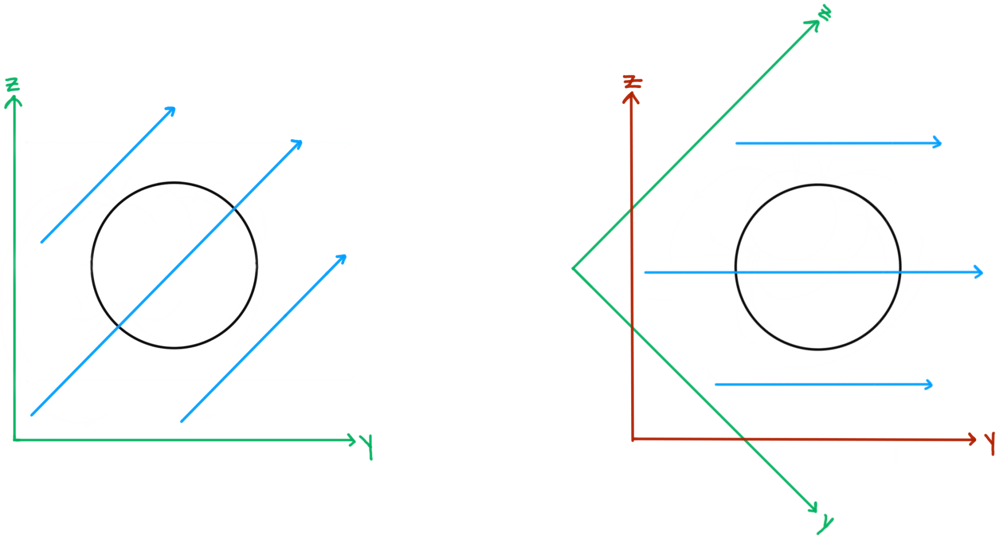

Figure 6.2: Schematic illustration showing the coordinate system transformation for the unmagnetized case for changing IMF (blue) orientations.

50 nT As seen in Figure 6.1, ion escape rates increase with increasing clock angle for a planetary dipole strength of 50 nT case for both O^+ and O_2^+. This increase corresponds to the opening of the magnetosphere as the IMF progresses from parallel to antiparallel to the dipole field lines Closed magnetospheric configurations have the lowest escape rates, while open configurations have an increase in escape. The O^+ escape rate for 50 nT is $8.45 \times 10^{24}\ s^{-1} \pm\ 10.1\%$ and the O_2^+ escape rate is $1.23 \times 10^{25}\ s^{-1} \pm\ 9.4\%$. The O_2^+ escape rate is higher than the O^+ escape rate due to the simulation injection parameters, described in detail in Chapter 2. The weakly magnetized case has the highest escape rate variation across all dipole field strengths when the IMF clock angle is changed.

100 nT For the magnetized planet, there is an increase in escape rate for both O^+ and O_2^+ with increasing clock angle, just like in the weakly magnetized case. The O^+ escape rate is $8.33 \times 10^{24}\ s^{-1} \pm\ 9.1\%$, which has a lower variation as compared to the 50 nT case. The O_2^+ escape rates also increase with increasing clock angle, corresponding to the opening of the magnetosphere as the IMF becomes antiparallel with the dipole field. The O_2^+ escape rate is $1.28 \times 10^{25}\ s^{-1} \pm\ 8.5\%$, which has a smaller variation than the O^+ escape rate.

Comparison of 50 nT and 100 nT The magnetized escape rates for O^+ are surpassed by those in the weakly magnetized case a clock angle of 0° and then are consistently lower as the clock angle increases. At this configuration, where the IMF is perpendicular to the dipole axis (IMF is completely in the +y direction), the O^+ escape rates for the dipole strengths of 50 nT and 100 nT are consistent with those found in Egan et al. (2019) [9].

As the IMF becomes antiparallel with the dipole axis (along the +z axis) and the magnetosphere opens up, O^+ escape rates for a dipole strength of 50 nT surpass those of the 100 nT case. This is because the weakly magnetized case does not supply as many closed field lines with its weaker dipole field strength as compared to the magnetized case, as shown in Figure 6.3. Thus, escape rates are higher at antiparallel IMF orientations for 50 nT than 100 nT, as shown through the O^+ flux in Figure 6.3 and in the escape rates in Figure 5.1.

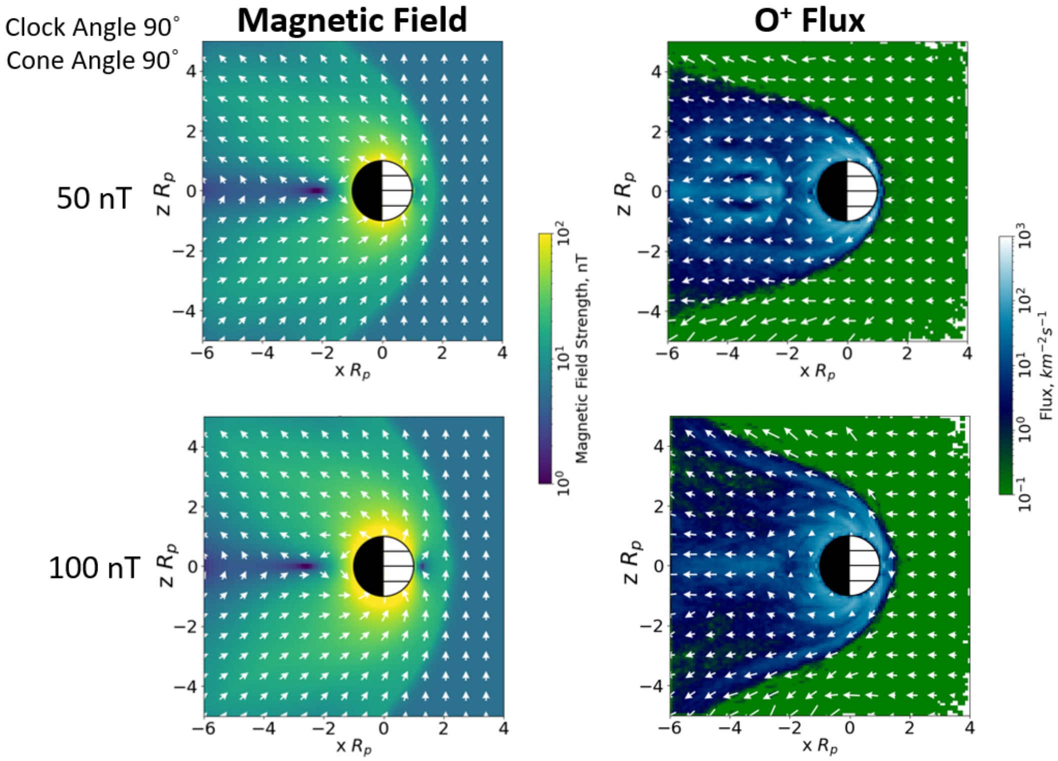

Figure 6.3: Plots comparing the 50 nT (top) dipole field strength to the 100 nT dipole field strength (bottom) with respect to magnetic field structure (left) and O$^+$ flux with velocity quivers (right).

6.2 Cone Angle Dependence

0 nT The unmagnetized case has a higher variation in escape rates when the cone angle changes, with an O^+ escape rate of 5.61×10^{24} s^{-1} $\pm$ 3.0% and an O_2^+ escape rate of 7.11×10^{24} s^{-1} $\pm$ 14.8%. Escape rates are roughly equal and highest with parallel IMF conditions, or in other words, when the IMF is parallel to the solar wind direction at cone angles 0° and 180°. This is due to the lack of solar wind convection electric field in the upstream region of the planet. The lack of convection electric field allows the ions to gyrate around the planetary open magnetic field lines, which increases the ion escape rates in these regions. Ion escape rates are lowest for O^+ and O_2^+ with a cone angle of 90° because the perpendicular IMF (all along the +y direction) induces a clearly defined magnetosphere, allowing for the planet to effectively 'hang on' to the O^+ and O_2^+ in its atmosphere. A comparison of magnetospheric structures and O^+ fluxes are shown in Figure 6.5, displaying the symmetry of O^+ escape flux on the dayside at parallel IMF orientations and the efficiently trapped O^+ when the IMF is perpendicular.

50 nT The presence of a weak intrinsic dipole field changes the trend of the escape rates. The weakly magnetized case has an O^+ escape rate of 8.45×10^{24} s^{-1} $\pm$ 9.6% and an O_2^+ escape rate of 1.23×10^{25} s^{-1} $\pm$ 9.4%. The trend with the escape rates is symmetric about a cone angle of 90°, but in the opposite manner of the unmagnetized case.

Because the solar wind convection field vanishes with parallel IMF, there is upstream escape as the ions are confined to gyrate around the magnetic field lines in that region, as shown in the left column of Figure 6.6. However, now that there is an intrinsic dipole field, there are closed planetary magnetic field lines that trap the planetary ions. Because the dipole field is the dominant factor in ion escape in this case, ion escape will be at a minimum as compared to the non-parallel IMF orientations.

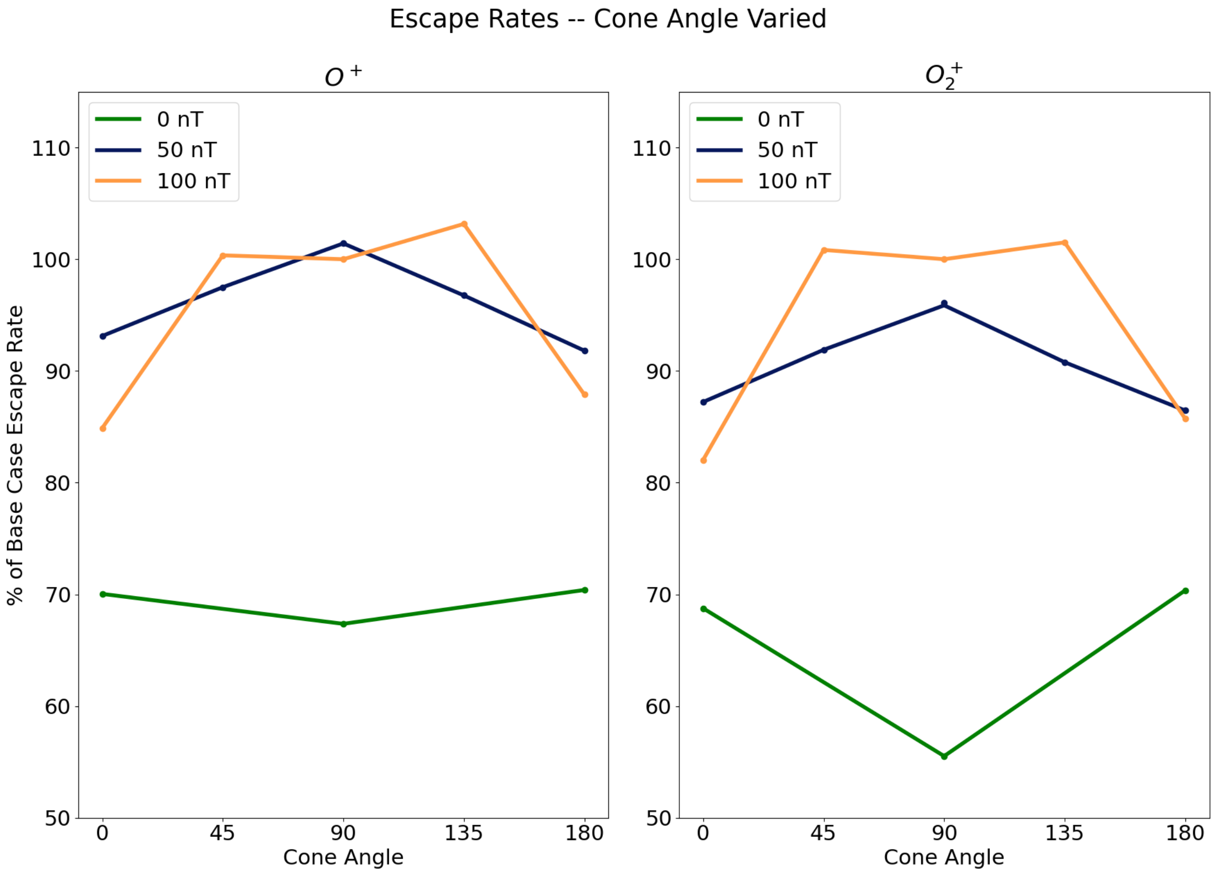

Figure 6.4: Plots comparing the 0 nT (green), 50 nT (purple), and 100 nT (orange) escape rate trends with changing cone angle for O^+ (left) and O_2^+ (right). Escape rates are presented as a percentage of the base case escape rates, defined in Chapter 3.

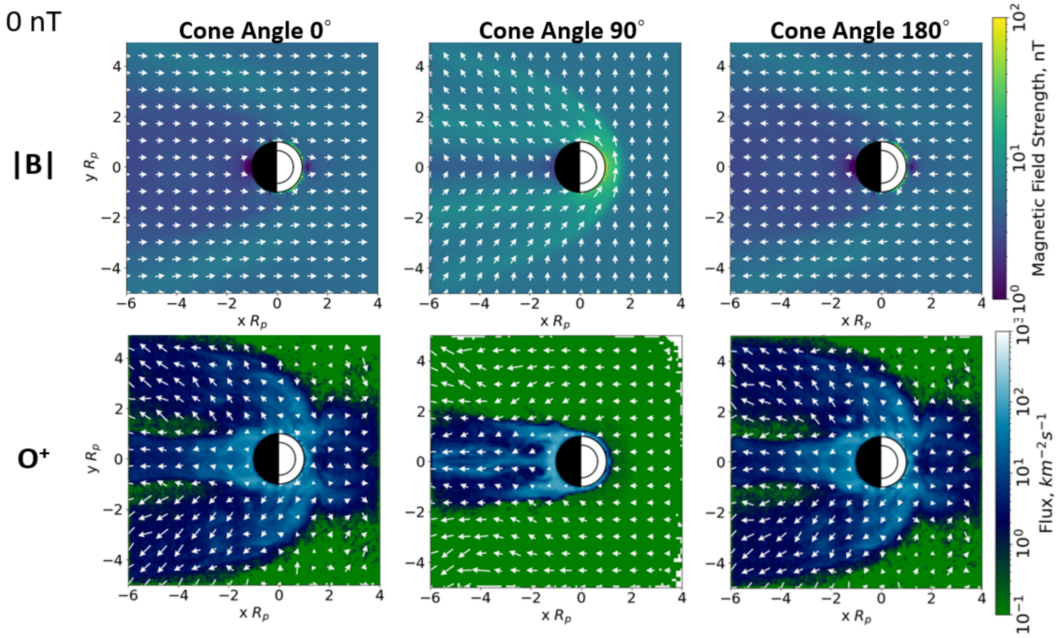

Figure 6.5: Plots showing the symmetry of magnetic field structure (top) and O$^+$ fluxes (bottom) with velocity quivers for the unmagnetized case through cone angles 0°, 90°, and 180°.

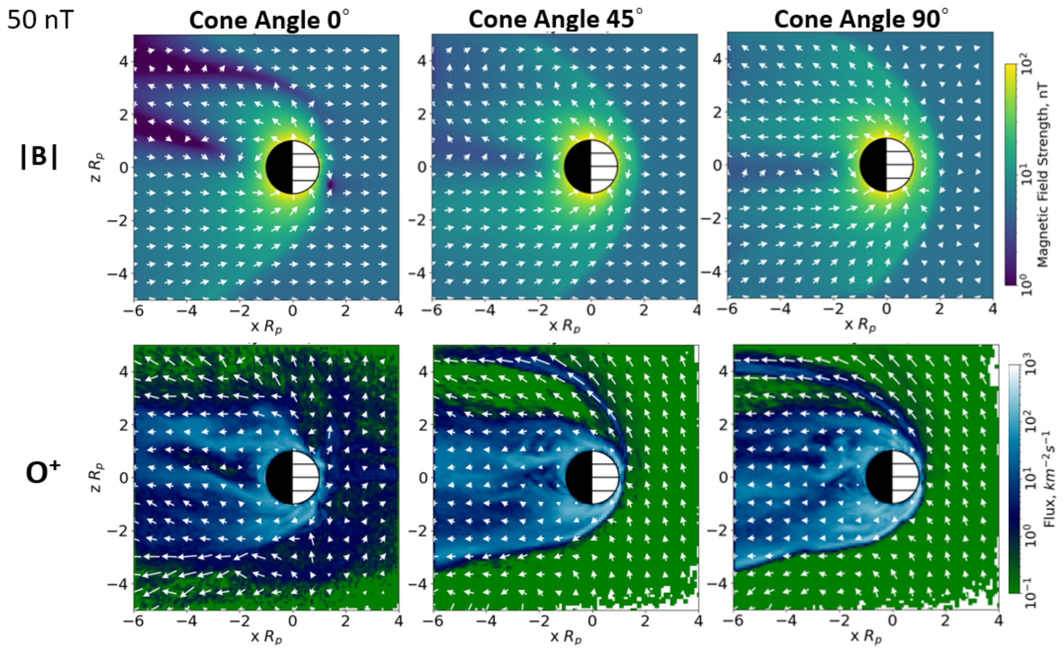

Figure 6.6: Plots showing the evolution of magnetic field structure (top) and increase of O$^+$ fluxes (bottom) with velocity quivers for the weakly magnetized case through cone angles 0°, 45°, and 90°.

As the clock angle increases to 90°, the convection electric field produces a plume on the dayside of the planet, accelerating ions out of the atmosphere, thereby increasing the escape rates. Escape through the plume is connected to the strength of the electric field, which is strongest at a cone angle of 90°, corresponding to the highest escape rates. As the clock angle increases to 180°, the convection electric field strength decreases and so do the escape rates.

100 nT The symmetry of ion escape rates is still observed when the magnetized case is considered, but with a different morphology. The escape rates for O^+ and O_2^+ in the 100 nT case are $8.33 \times 10^{24}\ s^{-1} \pm\ 15.1\%$ and $1.28 \times 10^{25}\ s^{-1} \pm\ 18.0\%$ respectively. For O^+ and O_2^+, as seen in Figure 6.4, the escape are roughly symmetric about a cone angle of 90°. Escape rates at 45° and 135° are higher than those at 90°, and the escape rates for radial IMF (cone angle 0° and 180°) are the lowest. Escape rates for the magnetized case are consistently higher than those in the weakly magnetized case, except for when the IMF is radial for both O^+ and O_2^+ and at a cone angle of 90° for O^+.

This is because the magnetized planet has a closed magnetosphere throughout the cone angle variation due to its stronger intrinsic dipole field, as discussed in the Chapter 5. Though there are more closed magnetic field lines that are able to trap the planetary ions, the ion escape rates for the magnetized case are higher than those in the weakly magnetized case. However, when the radial IMF cases are considered, the planetary dipole field is responsible for the ion acceleration instead of the solar wind generated convection electric field [9]. Therefore, escape rates are lowest for these IMF configurations, as expected.

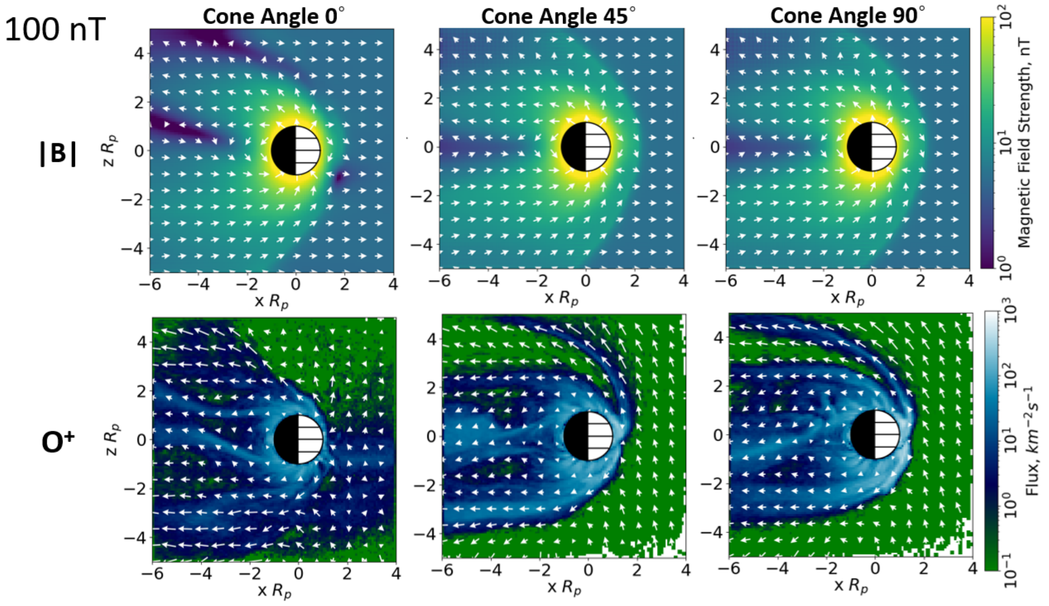

Figure 6.7: Plots showing the evolution of magnetic field structure (top) and increase of O^+ fluxes (bottom) with velocity quivers for the magnetized case through cone angles 0°, 45°, and 90°.

Chapter 7

Conclusion

Several planetary and stellar properties may influence a planet's habitability. In this project, we have focused the IMF orientation and planetary dipole field strength dependence on the magnetospheric structure and ion escape rates by manipulating one parameter at a time. We began with a 'base case' of a dipole field strength of 100 nT and an IMF orientation that is perpendicular to the dipole field axis, providing the basis for comparison through the study.

7.1 Summary of Results

Here, we summarize the findings of the study through each parameter analyzed.

Clock Angle Dependence on Ion Escape

- The magnetospheric boundaries change with an increase of clock angle. The magnetospheric structure begins with symmetric features at a clock angle of -90° and becomes asymmetric as the IMF clock angle increases to 90°. The magnetosphere is pulled along the +y direction as the magnetospheric configuration opens up.
- The O^+ and O_2^+ fluxes increase as the clock angle approaches 90°, corresponding to the opening of the magnetosphere. The convection electric field is the main driver for the ion loss cloud morphologies and resulting atmospheric escape.

- Ion escape rates increase (almost) linearly with an IMF clock angle change from southward IMF (clock angle -90°) to northward IMF (clock angle 90°). Ion escape rates increase with the opening of the magnetosphere, as expected.

Cone Angle Dependence on Ion Escape

- IMF cone angle has no dramatic effect on magnetospheric configuration (open vs. closed). Instead, cone angle changes the magnetospheric boundaries and null field regions asymmetrically about a cone angle of 90° along the +z axis
- The atmospheric ion fluxes are roughly symmetric about a cone angle of 90°, with fluxes highest at a cone angle of 90° and lowest when the IMF is radial (cone angle 0° and 180°).
- Ion escape rates are symmetric about a cone angle of 90°, with the highest escape rates at a cone angles 45° and 135° and lowest when the IMF is radial.

Dipole Field Strength Dependence on Ion Escape

- Ion escape rates are lowest in the unmagnetized case and increase when an intrinsic dipole field is introduced.
- Escape rates for the unmagnetized case remain constant for changing clock angle. For changing cone angle, escape rates are highest for radial IMF.
- The weakly magnetized case (50 nT) has linearly increasing ion escape rates with increasing clock angle, surpassing the magnetized case O^+ escape rates when the IMF is perpendicular to the dipole field axis. Escape rates for changing cone angle are symmetric about a cone angle of 90°.
- Escape rates for the magnetized case have the highest variation of all dipole field strengths explored in this study.

7.2 Future Work

Moving forward, more work is needed to quantify the escape energies of O^+ and O_2^+ with changing IMF orientations and dipole field strengths to determine the magnitude of energization during atmospheric loss. Furthermore, expanding the simulation domain in the model would be useful to analyze the magnetospheric boundaries and ion loss clouds in the magnetotail. Running the model at higher resolution would provide higher accuracy for the model-calculated escape rates and exhibit finer detail of charged particle motions in the simulation. Expanding the study past just IMF orientation by manipulating the strength of the field in the solar wind or altering the solar wind initial conditions to reflect solar maximum would provide insight as to which stellar conditions correspond to atmospheric retention.

Bibliography

[1] S. Barabash, A. Fedorov, J. J. Sauvaud, R. Lundin, C. T. Russell, Y. Futaana, T. L. Zhang, H. Andersson, K. Brinkfeldt, A. Grigoriev, and et al. The loss of ions from Venus through the plasma wake. Nature, 450(7170):650–653, 2007.

[2] Markus Battarbee, Otto Akseli Hannuksela, Yann Pfau-Kempf, Sebastian von Alfthan, Urs Ganse, Riku Jarvinen, Leo, Jonas Suni, Markku Alho, lturc, Ilja, tvbrito, and Maxime Grandin. fmihpc/analysator: v0.9, January 2021.

[3] D. A. Brain, F. Bagenal, Y.-J. Ma, H. Nilsson, and G. Stenberg Wieser. Atmospheric escape from unmagnetized bodies. Journal of Geophysical Research: Planets, 121(12):2364–2385, 2016.

[4] D. A. Brain, J. P. McFadden, J. S. Halekas, J. E. P. Connerney, S. W. Bougher, S. Curry, C. F. Dong, Y. Dong, F. Eparvier, X. Fang, K. Fortier, T. Hara, Y. Harada, B. M. Jakosky, R. J. Lillis, R. Livi, J. G. Luhmann, Y. Ma, R. Modolo, and K. Seki. The spatial distribution of planetary ion fluxes near Mars observed by MAVEN. Geophysical Research Letters, 42(21):9142–9148, 2015.

[5] Imke de Pater and Jack J. Lissauer. Magnetic Fields and Plasmas, page 283–336. Cambridge University Press, 2 edition, 2015.

[6] Y. Dong, X. Fang, D. A. Brain, J. P. McFadden, J. S. Halekas, J. E. P. Connerney, F. Eparvier, L. Andersson, D. Mitchell, and B. M. Jakosky. Seasonal variability of Martian ion escape through the plume and tail from MAVEN observations. Journal of Geophysical Research: Space Physics, 122(4):4009–4022, 2017.

[7] E. Dubinin, R. Modolo, M. Fraenz, M. Päetzold, J. Woch, L. Chai, Y. Wei, J. E. P. Connerney, J. Mcfadden, G. DiBraccio, J. Espley, E. Grigorenko, and L. Zelenyi. The induced magnetosphere of Mars: Asymmetrical topology of the magnetic field lines. Geophysical Research Letters, 46(22):12722–12730, 2019.

[8] Hilary Egan, Riku Jarvinen, and David Brain. Stellar influence on heavy ion escape from unmagnetized exoplanets. Monthly Notices of the Royal Astronomical Society, 486(1):1283–1291, 03 2019.

[9] Hilary Egan, Riku Jarvinen, Yingjuan Ma, and David Brain. Planetary magnetic field control of ion escape from weakly magnetized planets. Monthly Notices of the Royal Astronomical Society, 488(2):2108–2120, 07 2019.

[10] B. M. Jakosky, R. P. Lin, J. M. Grebowsky, J. G. Luhmann, D. F. Mitchell, G. Beutelschies, T. Priser, M. Acuna, L. Andersson, D. Baird, and et al. The Mars Atmosphere and Volatile Evolution (MAVEN) mission. Space Science Reviews, 195(1-4):3–48, 2015.

[11] R. Jarvinen, D. A. Brain, R. Modolo, A. Fedorov, and M. Holmström. Oxygen ion energization at Mars: Comparison of MAVEN and Mars Express observations to global hybrid simulation. Journal of Geophysical Research: Space Physics, 123(2):1678–1689, 2018.

[12] Yingjuan Ma, Andrew F. Nagy, Igor V. Sokolov, and Kenneth C. Hansen. Three-dimensional, multispecies, high spatial resolution MHD studies of the solar wind interaction with Mars. Journal of Geophysical Research: Space Physics, 109(A7), 2004.

[13] M. Persson, Y. Futaana, R. Ramstad, K. Masunaga, H. Nilsson, M. Hamrin, A. Fedorov, and S. Barabash. The Venusian atmospheric oxygen ion escape: Extrapolation to the early solar system. Journal of Geophysical Research: Planets, 125(3):e2019JE006336, 2020. e2019JE006336 2019JE006336.

[14] Robin Ramstad and Stas Barabash. Do intrinsic magnetic fields protect planetary atmospheres from stellar winds? Space Science Reviews, 217(2), Mar 2021.

[15] Robin Ramstad, Stas Barabash, Yoshifumi Futaana, Hans Nilsson, Xiao-Dong Wang, and Mats Holmström. The Martian atmospheric ion escape rate dependence on solar wind and solar EUV conditions: 1. Seven years of Mars Express observations. Journal of Geophysical Research: Planets, 120(7):1298–1309, 2015.

[16] Shotaro Sakai, Kanako Seki, Naoki Terada, Hiroyuki Shinagawa, Ryoya Sakata, Takashi Tanaka, and Yusuke Ebihara. Effects of the IMF direction on atmospheric escape from a Mars-like planet under weak intrinsic magnetic field conditions. Journal of Geophysical Research: Space Physics, 126(3):e2020JA028485, 2021.

[17] Shotaro Sakai, Kanako Seki, Naoki Terada, Hiroyuki Shinagawa, Ryoya Sakata, Takashi Tanaka, and Yusuke Ebihara. Enhanced ion escape rate during IMF rotation under weak intrinsic magnetic field conditions on a Mars-like planet. Journal of Geophysical Research: Space Physics, 128(3):e2022JA030510, 2023. e2022JA030510 2022JA030510.

[18] Shotaro Sakai, Kanako Seki, Naoki Terada, Hiroyuki Shinagawa, Takashi Tanaka, and Yusuke Ebihara. Effects of a weak intrinsic magnetic field on atmospheric escape from Mars. Geophysical Research Letters, 45(18):9336–9343, 2018.

[19] Victoria Simpson. Reasons why the Earth's magnetic field is extremely useful, Jul 2020.